COMPUTER SIMULATIONS OF EXCITATIONS OF A QUANTUM SOLID AND OF THE MELTING TRANSITION AT HIGH PRESSURE

VIACHESLAV SORKIN

COMPUTER SIMULATIONS OF EXCITATIONS OF A QUANTUM SOLID AND OF THE MELTING TRANSITION AT HIGH PRESSURE

RESEARCH THESIS

SUBMITTED IN PARTIAL FULFILLMENT OF THE

REQUIREMENTS

FOR THE DEGREE OF DOCTOR OF PHILOSOPHY

VIACHESLAV SORKIN

SUBMITTED TO THE SENATE OF THE TECHNION — ISRAEL INSTITUTE OF TECHNOLOGY

TISHREI, 5767 HAIFA OCTOBER, 2006

THIS RESEARCH THESIS WAS SUPERVISED BY DR. JOAN ADLER AND PROF. EMIL POLTURAK UNDER THE AUSPICES OF THE PHYSICS DEPARTMENT

ACKNOWLEDGMENT

I wish to express my gratitude to J. Adler and E. Polturak for the excellent guidance and support during this research.

I am grateful to D. M. Ceperley for providing me with his UPI9CD PIMC code. I was benefited from several discussions with N. Gov, S. Moroni, D. Landau and E. Tadmor. I wish to thank to A. Sorkin, O. Peleg, S. Meni, N. Schreiber and T. Mutat for their help during the research period.

I would like to express my gratitude to A. Weil for the help on the IUCC machines and parallel computing. I also thank the IUCC for allowing me CPU time on their linux-cluster and the Silicon Graphics supercomputer of the Technion.

THE GENEROUS FINANCIAL HELP OF THE TECHNION AND ARTHUR M. SILLS DOCTORAL FELLOWSHIP IS GRATEFULLY ACKNOWLEDGED

Contents

List of Figures

List of Tables

Abstract

The behavior of solids depends on the motion of their atoms which can be studied by simulations. Simulations allow us to gain a better understanding of the properties of solids, by providing a link between atomic scales and macroscopic phenomena.

The subject of the first part of the thesis is excitations in solid helium. Solid helium is characterized by large zero-point motion and significant correlation of its atoms. The self - consistent phonon (SCP) theory [1], which accounts these properties, has been developed over the years. The predictions of the SCP agree well with experiment in high-density phases. In the low-density bcc phase, the agreement is less satisfactory. As a complementary approach to the SCP, we decided to use numerical methods (Path Integral Monte Carlo in conjuction with Maximum Entropy [2] technique) to study the dynamics of solid helium in bcc phase.

We calculated the dynamic structure factor, $S(\mathbf{q},\omega)$, of solid ^{4}He at a molar volume of 21 cm^3 and solid ^{3}He at a molar volume of 21.5 cm^3 at a temperature 1.6 K. Both the single-phonon contribution to the dynamic structure factor and the total $S(\mathbf{q},\omega)$ were evaluated. From $S(\mathbf{q},\omega)$ we obtained the phonon spectra and found good agreement between our results and experimental data for ^{4}He and the theoretical prediction [3] for ^{3}He.

Melting at high pressure is the subject of the second part of the thesis. Systematic

differences exist in experimental results on the melting temperature measured at high pressures using the diamond anvil cell (DAC) and the shock wave technique [4]. The melting temperature, T_m, determined using shock waves is systematically higher than that obtained by extrapolation of DAC measurements.

Several explanations were proposed to resolve this discrepancy, including the existence of an extra high P-T phase and an overshoot of the T_m in shock-wave experiments [4]. We noticed that no attention was devoted to the different conditions which exist at the surface of the samples in the experimental methods. Inside a DAC, the sample is surrounded by a hydraulic medium. In shock-wave experiments, the molten region of the sample is bordered by unstressed cold regions. In both cases, the sample has no free surface, which play a crucial role in the melting transition at zero pressure [5, 6].

Therefore, we decided to study how the different types of boundary conditions may affect the melting transition at high pressures. A model system of argon atoms with different conditions specified at its surface was simulated using Monte Carlo method. We examined two cases: in the first case the argon was in contact with a rigid wall and in the second case with a fluid neon layer.

Our results showed that T_m is systematically different in the two cases. We found that in the presence of a rigid medium, melting resembles the mechanical instability found in a surface-free solid. With a soft medium at the boundary, melting begins at the surface and at a lower temperature. These results are related to experiments and appear to be consistent with systematic differences that exist between shock wave and DAC measurements. We suggest that results obtained with a DAC technique should be compared with thermodynamic theories, while shock wave results should be compared with theories based on a mechanical instability.

List of symbols

T	temperature
P	pressure
V	volume
N	number of atoms
S	entropy
E	energy
H	Hamiltonian
Z_N	partition function
F	Helmholtz free energy
G	Gibbs free energy
T_m	melting temperature
k_B	Boltzmann constant
β	inverse temperature
$\mathbf{q}$	wavevector
τ	imaginary time
λ	phonon polarization
ω	phonon energy

$S(\mathbf{q},\omega)$	dynamic structure factor
$S_1(\mathbf{q},\omega)$	single phonon dynamic structure factor
$F(\mathbf{q},\tau)$	intermediate scattering function
a	lattice constant
Ψ	wave function
Ψ_G	ground state wave function
$f_J(r)$	Jastrow function
ρ	number density
i,j,l	particle indeces
x,y,z	the three Cartesian coordinates
$\alpha,\beta,..$	Cartesian indeces
$\mathbf{r}_i$	position of atom i
$\mathbf{u}_i$	deviation of atom i from its lattice site
$[\mathbf{r}]$	coordinates of N atoms
$\Phi^{ij}_{\alpha,\beta}$	force constants
$d^{ij}_{\alpha,\beta}$	one phonon propagator
$g(ij,rt)$	pair correlation function
ΔE_v	vacancy formation energy
DAC	Diamond Anvil Cell
MC	Monte Carlo
LJ	Lennard Jones potential
$MaxEnt$	Maximum Entropy Method
$PIMC$	Path Integral Monte Carlo
$PIGS$	Path Integral Ground State Monte Carlo
SCH	Self Consistent Harmonic Theory
SCP	Self Consistent Phonon Theory
SWF	Shadow Wave function
SW	Shock Wave

Chapter 1

Phonons in solid helium

In this chapter we discuss some dynamical properties of solid helium observed in neutron scattering experiments and the theories used to describe these properties. We begin with the measurements of phonon spectra by the Brookhaven group. Then we outline the different theoretical methods developed to calculate the phonon spectrum in ^{4}He. The self-consistent phonon theory, renormalization phonon theory and quantum Monte Carlo method based on Shadow Wave Function are described in detail in the following paragraphs.

1.1 Theory and experiment

Solid ^{4}He is the most prominent example of a quantum solid. It displays highly anharmonic dynamics: its atoms are loosely bound, make large excursions to the nearest neighbor sites and are strongly correlated. The root-mean square (RMS) vibration amplitude of helium atoms is about 30% of the lattice spacing. For comparison, classical solids melt when the RMS vibration amplitude is about 10% of the lattice

parameter [14]. The kinetic energy per atom in the bcc phase is so large that the lattice constant of the crystal is expanded beyond the inflection point of the interatomic potential, e.g. helium atoms reside in a double well potential. This double well potential is illustrated in Fig. 1.1 and compared with a parabolic potential typical for classical solids (see Fig. 1.2). To draw these Figures we approximated the interatomic potential by a Lennard - Jones (6-12) potential and took the experimental value for the lattice parameter [1].

The first calculations [15], based on harmonic approximation, yielded imaginary phonon frequencies. According to the Born criterion [16] solid bcc ^{4}He should melt due to mechanical instability of its lattice. These results motivated the first experimental studies of phonons in the bcc phase of ^{4}He.

The Brookhaven group [17, 18, 19] observed phonons in the bcc ^{4}He using inelastic neutron scattering. In these experiments neutrons penetrated deep into the sample and underwent scattering by transferring momentum and energy to the crystal lattice. The angular distribution and energy of the neutrons emerging from the crystal were measured to construct the phonon dispersion curves (See Fig. 1.3).

It was found that for large molar volume crystals (V = 21 cm^3/mol) the lattice dynamics of bcc ^{4}He is "decidedly non-classical" [17]: the phonon group profiles are often significantly distorted from the Gaussian contour and not identical at symmetry-related positions in reciprocal space (See Fig. 1.4).

The experiments clearly demonstrated that phonons do exist in the bcc phase of ^{4}He, although they cannot be described by a harmonic approximation of non-interacting phonons. Anharmonicity, an inherent property of quantum crystals, gives rise to interaction between the phonons. For classical solids, the anharmonic effects are usually negligible and taken into account as low order perturbation corrections.

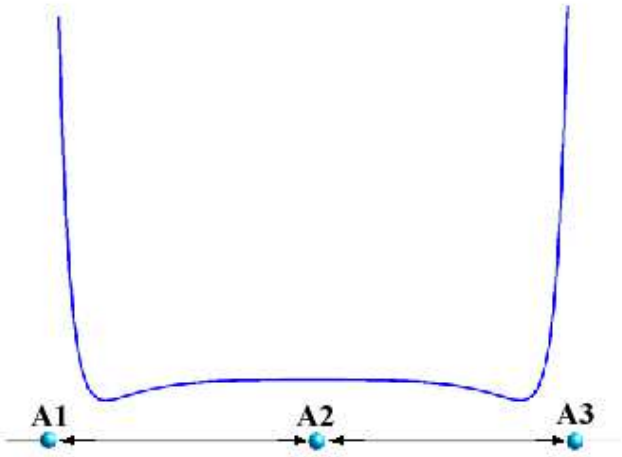

Figure 1.1: Double well structure of the total potential in a quantum solid.

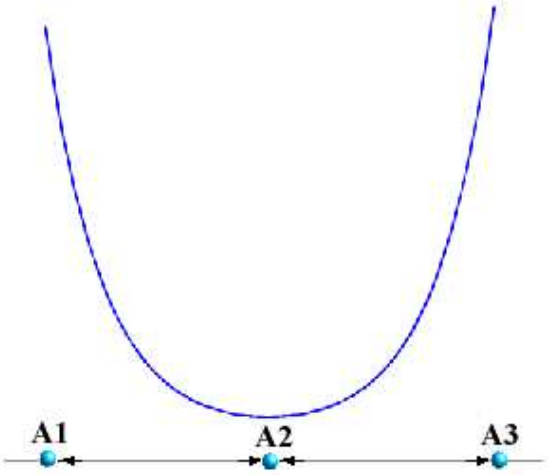

Figure 1.2: The total potential in a "classical" solid. This potential can be approximated by a quadratic functions.

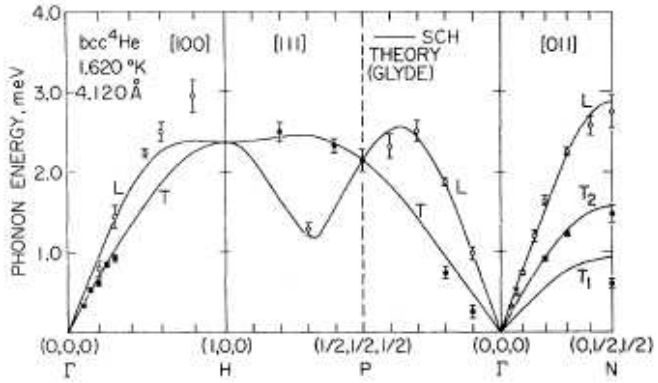

Figure 1.3: Experimental dispersion curves [18] for bcc ^{4} He at V = 21 cm^3/mol and T = 1.62 K. The solid circles indicate transverse branches. The open circles indicate longitudinal branches. The solid lines represent the first-order theory of Glyde [1].

For quantum solids the anharmonic effects are significant and new approaches were developed to treat them. An inter-atomic potential was replaced by an effective pair-potential averaged over the motions of neighbor atoms and short range atomic correlations were introduced.

Various theoretical methods were proposed: Glyde et al. [1, 20, 21] developed the self - consistent phonon (**SCP**) theory (described in detail below). In this theory the force constants and phonon frequencies are determined in a self-consistent way and the short range correlations are taken into account by Jastrow functions.

Koehler and Werthamer [23] proposed a variational technique related to the Feynman [24] theory of liquid helium. By applying a variational Gaussian set (which incorporates the short range correlations) and an effective potential they calculated the phonon spectrum at zero temperature. The high-order anharmonicity was included by using two- and three-phonon modes in the variational basis set.

Horner [28, 29] applied the many-body perturbation technique to obtain the

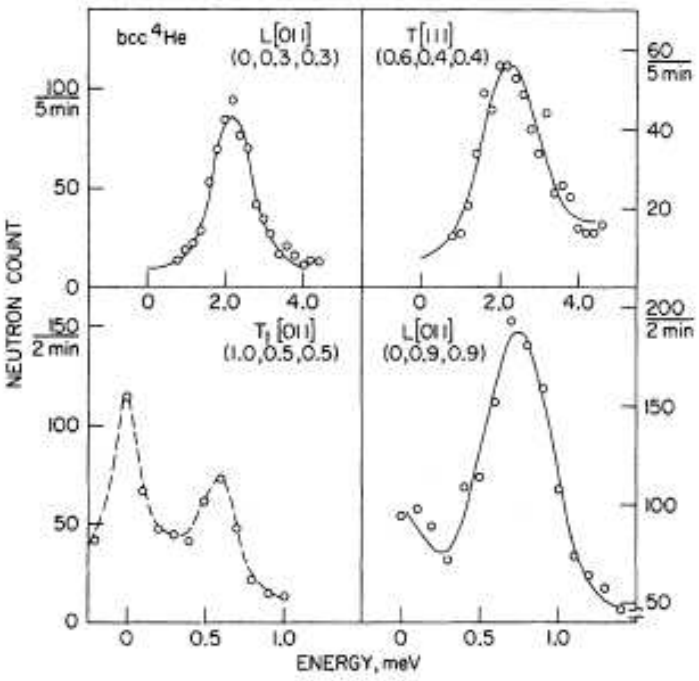

Figure 1.4: Phonon groups for low energy phonons in bcc ^{4} He observed by Osgood et al. [18] at molar volume V = 21 cm^3 and temperature T = 1.62 K.

phonon spectrum in solid helium. His approach (described in detail below) is considered as the most general method [1] based on the formalism of the time-dependent Green functions and the variational technique. It includes in a systematic and self-consistent way the effects of anharmonicity and the short range correlations. The overall agreement between Horner's theory and experiments is of order of $\pm 20\%$.

Recently, the phonon spectrum was calculated by using time-dependent random phase approximation [25, 26], and the density functional method [27] (in the vicinity of the melting temperature). Reatto et al. [13] applied Quantum Monte Carlo to calculate the spectrum of longitudinal phonons at zero temperature.

Finally, in order to reconcile the theory and the experiment Gov et al. [11] conjectured the existence of a new type of excitations (local modes) in the bcc phase.

The local modes interact only with the transverse phonons and modify the problematic transverse branch $T_1[011]$, marked by significant discrepancy between the SCP predictions and experimental measurements [11].

The second isotope of solid helium, ^{3}He, is another prominent example of a quantum solid [1, 30]. In contrast to ^{4}He, there are no experimental measurements of phonon spectra of ^{3}He (in the bcc phase) due to the large neutron absorption cross-section of this isotope. [1, 31] Recently, however, the use of inelastic X-ray scattering [32, 33] offers the possibility of experimentally determining the phonon branches of ^{3}He. In addition, new neutron scattering experiments are being planned, [34, 35] which will be able to acquire data for a sufficiently long time to observe inelastic scattering. These developments have motivated the our study of dynamics of ^{3}He.

Several theoretical methods, developed for ^{4}He, have been applied to investigate dynamics of ^{3}He: Glyde and Khanna devised a self-consistent phonon formalism [3], Horner developed a many-body perturbation technique [28, 36], and Koehler and Werthamer employed a variational approach [23]. These theoretical calculations are based on a variational perturbative theory and implemented at zero-temperature [1]. The predictions of these models are in quantitative disagreement with each other, due to differences in the effective potentials used to evaluate phonon interactions and details of the numerical methods employed [23]. As a complementary approach to these methods we decided to study the excitations in bcc solid helium by performing Quantum Monte Carlo simulations.

1.2 Self Consistent Phonon Theory

The self consistent phonon theory is an elegant and pragmatic method for calculation of phonon spectrum of solid helium. The method can be introduced heuristically as a generalization of a standard perturbation theory, which is used when anharmonic effects are small.

In the framework of a standard perturbation theory one begins by expanding the total potential, V([**r**])=$\sum_{l<l'} v(r_{ll'})$, in a power series of the displacements:

$$V([\mathbf{r}]) = V([\mathbf{R}]) + \frac{1}{2}\sum_{\alpha,\beta} \Phi^{ll'}_{\alpha\beta} u^l_\alpha u^{l'}_\beta + \frac{1}{6}\sum_{\alpha,\beta,\gamma} \Phi^{ll'l''}_{\alpha\beta\gamma} u^l_\alpha u^{l'}_\beta u^{l''}_\gamma + ... \tag{1.1}$$

where $v(r_{ll'})$ is a pair potential, l denotes an atom at l-crystalline site, $r_{ll'} = |\mathbf{r}_l - \mathbf{r}_{\mathbf{l'}}|$ is the distance between l and l' atoms, and α, β, γ are Cartesian indeces. We denote by $[\mathbf{r}] = \{\mathbf{r_1}, \mathbf{r_2}, ..., \mathbf{r_N}\}$ all atomic coordinates, and by $[\mathbf{R}] = \{\mathbf{R_1}, \mathbf{R_2}, ...\mathbf{R_N}\}$ their equilibrium positions (lattice sites). The displacement of an atom from its lattice site is $u^l_\alpha = r^l_\alpha - R^l_\alpha$, and $\Phi^{ll'}_{\alpha\beta}$ are force constants, e.g. derivatives of the total potential V([**r**]) calculated at R^l_α according to:

$$\Phi^{ll'}_{\alpha\beta} = \nabla^l_\alpha \nabla^{l'}_\beta v(R_{ll'}) \tag{1.2}$$

where $R_{ll'} = |\mathbf{R_l} - \mathbf{R_{l'}}|$. The harmonic approximation is then obtained by truncating the series (1.1) beyond the second term. This gives the following equations of motion:

$$M\ddot{u}^l_\alpha = -\sum_{l',\beta} \Phi^{ll'}_{\alpha\beta} u^{l'}_\beta \tag{1.3}$$

The phonon spectrum can be calculated by a transformation to the normal coordinates, $\mathbf{A}(\mathbf{q}, \lambda, t)$ [1]:

$$u^l_\alpha(t) = \frac{1}{\sqrt{NM}} \sum_{\mathbf{q},\lambda} A(\mathbf{q}, \lambda, t)\epsilon_\alpha(\mathbf{q}, \lambda) \tag{1.4}$$

where phonon polarizations (longitudinal and transversal modes) is denoted by λ, $\mathbf{q}$ is the reciprocal lattice vector, $\epsilon_\alpha(\mathbf{q},\lambda)$ is the set of unit polarization vectors and N is the number of atoms.

Assuming an oscillatory dependence of the normal coordinate on time $\mathbf{A}(\mathbf{q},\lambda,t) \sim \exp(-i\omega_{\mathbf{q},\lambda}t)$, the phonon frequencies, $\omega_{\mathbf{q},\lambda}$ are given by:

$$\omega^2_{\mathbf{q},\lambda} = \sum_{\alpha,\beta} \epsilon_\alpha(\mathbf{q},\lambda)\epsilon_\beta(\mathbf{q},\lambda) \sum_{l,l':l\neq l'} \Phi^{ll'}_{\alpha\beta}(\exp(i\mathbf{q}\mathbf{R}_{ll'}) - 1). \tag{1.5}$$

This expression for $\omega_{\mathbf{q},\lambda}$ is valid only if atomic displacements are small comparing to the average interatomic distance. This condition does not hold in the bcc phase of ^{4}He. Even if the atomic displacements were small the phonon frequencies still could not be obtained with (1.5), since in the bcc phase atoms reside at the local maxima of the potential (See Fig. 1.1). In this case the force constants (1.2) are negative $\Phi^{ll'}_{\alpha\beta} < 0$ and consequently $\omega^2_{\mathbf{q},\lambda} < 0$.

The principal error of this approach is the evaluation of $\Phi^{ll'}_{\alpha\beta}$ at the atomic equilibrium positions, as if atoms are fixed at their lattice sites. The more physically reasonable approach is to calculate the force constants by taking the average of the second derivatives over the region of space accessible by the atom. In the SCP theory, the force constants are re-defined by averaging over pair correlation function according to:

$$\Phi^{ll'}_{\alpha\beta} \rightarrow \Phi^{ll'}_{\alpha\beta} = \int g(ll',rt)\nabla^l_\alpha \nabla^{l'}_\beta v(r_{ll'})dr_{ll'} \tag{1.6}$$

where $g(ll',rt)$ is (unknown) pair correlation function, which is defined as:

$$g(ll',rt) =< \delta(r - r_{ll'}) > \tag{1.7}$$

using a Fourier transformation $g(ll',rt)$ can be also written as:

$$g(ll',rt) = \int \frac{d^3k}{(2\pi)^3} e^{i\mathbf{k}\mathbf{r}} < e^{i\mathbf{k}\mathbf{r}_{\mathbf{ll'}}} > \tag{1.8}$$

The $< e^{i\mathbf{k}\mathbf{r}_{\mathbf{ll'}}} >$ term then is expanded in a series (cumulant expansion) [1]:

$$< \exp i\mathbf{k}\mathbf{r}_{\mathbf{ll'}} >= \exp(\sum_n \frac{(-i)^n}{n!} M_n) \tag{1.9}$$

where M_n is n cumulant. For example, the first and the second cumulants are given by:

$$M_1 =< \mathbf{k}\mathbf{r}_{\mathbf{ll'}} >=< \mathbf{k}\mathbf{R}_{\mathbf{ll'}} >, \tag{1.10}$$

$$M_2 = 2k^2(< \mathbf{u_l}\mathbf{u_l} > - < \mathbf{u_l} >< \mathbf{u_{l'}} >) = 2k^2(< \mathbf{u_l}\mathbf{u_l} >), \tag{1.11}$$

The last identity is obtained by assuming a symmetric vibration distribution:

$$< \mathbf{u_l} >=< \mathbf{u_{l'}} >= 0 \tag{1.12}$$

If the cumulant series is truncated beyond the second term, the phonon frequencies are calculated in self-consistent harmonic (SCH) approximation.

The pair-correlation function $g(ll', rt)$ can be calculated using the time-dependent one-phonon correlation function:

$$d^{ll'}_{\alpha\beta}(t) =< u^l_\alpha(t) u^{l'}_\beta(0) > \tag{1.13}$$

The Fourier transform of this function

$$d_{\alpha\beta}(\mathbf{q}, \omega) = \sum_{l,l':l\neq l'} e^{-i\mathbf{g}\mathbf{R}_{\mathbf{ll'}}} \int_{-\infty}^{+\infty} dt e^{i\omega t} d^{ll'}_{\alpha\beta}(t) \tag{1.14}$$

is expressed in terms of the spectral function $A(\mathbf{q}, \lambda; \omega)$ according to:

$$d_{\alpha\beta}(\mathbf{q}, \omega) = (n_B(\omega) + 1) \sum_\lambda \frac{\hbar}{2M\omega_{\mathbf{q},\lambda}} \epsilon_\alpha(\mathbf{q}, \lambda)\epsilon_\beta(\mathbf{q}, \lambda) A(\mathbf{q}, \lambda; \omega) \tag{1.15}$$

where the Bose statistics is taken by $n_B(\omega) = (e^{\beta\hbar\omega} - 1)^{-1}$ into account ($\beta = 1/kT$). The frequency ω at which $A(\mathbf{q}, \lambda; \omega)$ has its maximum defines the frequency of a

phonon with given wave vector $\mathbf{q}$ and polarization λ. In the harmonic approximation, where the excitations are non-interacting phonons, the spectral function is given by [1]:

$$A(\mathbf{q},\lambda;\omega) = 2\pi\left(\delta(\omega-\omega_{\mathbf{q},\lambda}) - \delta(\omega+\omega_{\mathbf{q},\lambda})\right) \tag{1.16}$$

In solid helium, the phonons interact and this gives rise to a shift of their frequencies. The delta function $A(\mathbf{q},\lambda;\omega)$ of non-interacting phonons is broadened (see Fig. 1.4). The phonons have a finite lifetime, which is inversely related to the half-width of the spectral function.

If $A(\mathbf{q},\lambda;\omega)$ is known, then the equal-time phonon propagator can be expressed in terms of the spectral function

$$< u_\alpha^l(0)u_\beta^{l'}(0) >= \sum_{\mathbf{q},\lambda} \frac{\hbar}{MN\omega_{\mathbf{q},\lambda}} \left(1-e^{-i\mathbf{g}\mathbf{R}_{\mathbf{ll'}}}\right)\epsilon_\alpha\epsilon_\beta \int_{-\infty}^{+\infty}\frac{d\omega}{2\pi}(n_B(\omega)+1)A(\mathbf{q},\lambda;\omega). \tag{1.17}$$

Thereafter, the second cumulant M_2, can be calculated according to (1.11), where the atomic deviations are evaluated at the equal times, and finally the pair-correlation function, $g(ll',rt)$ is obtained.

We summarize the SCP method as following: to obtain the phonon frequencies, $\omega_{\mathbf{q},\lambda}$ by using (1.5), one has to calculate the force constants, $\Phi_{\alpha\beta}^{ll'}$. The $\Phi_{\alpha\beta}^{ll'}$ can be obtained if the pair-correlation function, $g(ll',rt)$ is known (see (1.7)). In the SCH $g(ll',rt)$ is expressed in terms of phonon propagator, which in turn depends on the (unknown) spectral function and the $\omega_{\mathbf{q},\lambda}$ (see (1.17)). If the spectral function is approximated by two delta functions (1.16), then the phonon spectrum can be calculated self-consistently. Usually, one begins with $\omega_{\mathbf{q},\lambda}$ for non-interacting (harmonic approximation) and iterates until consistent results are obtained.

The predictions of the SCH theory agree well with experiment in the fcc and hcp

solid phases. However, in the low-density bcc phase the agreement is less satisfactory [1, 11]. The success of the SCH for the moderately anharmonic fcc and hcp phases (molar volume V $\leq$ 12 cm^3/mol) is determine by the atomic vibrational distribution, which can be reasonably well approximated by a Gaussian. In solid helium with larger volume (V $\geq$ 12 cm^3/mol) the Gaussian approximation for the vibrational distribution is not valid. Since the vibrational amplitudes are very large, the Gaussian distribution has long tails, which allows atoms to approach each other nonphysically closely. As a result the pair distribution becomes nonphysically narrow and the $\omega_{\mathbf{q},\lambda}$ calculated with it lie above the experimental values.

The SCH can be improved either by going to higher order terms in the cumulant expansion (1.9) or by introducing explicitly short-range inter-atomic correlations. The calculations with higher order cumulants quickly became very tedious and converge too slowly to be useful [1]. Therefore, short-range correlations are introduced by multiplying the $g(ll', rt)$ by a Jastrow factor, $f_J(r)$. The Jastrow factor can be chosen as [1]:

$$f_J(r) = \exp(-Kv(r)/4\epsilon) \tag{1.18}$$

where K and ϵ are variational parameters, and $v(r)$ is a pair potential. By introducing the short-range correlations one effectively includes the higher order anharmonic terms in the vibrational distribution. The force constants obtained with the modified pair-correlation function are given by [1] :

$$\Phi^{ll'}_{\alpha\beta} = \frac{< \nabla^l_\alpha \nabla^{l'}_\beta w >}{< f_J^2 >} - \frac{< w >< \nabla^l_\alpha \nabla^{l'}_\beta f_J^2 >}{< f_J^2 >}, \tag{1.19}$$

where w is a new effective pair potential, which incorporates the short range correlations:

$$w(r) = f_J^2(r)(v(r) - \frac{\hbar^2}{2M}\Delta \ln f_J(r)) \tag{1.20}$$

The phonon frequencies are calculated according to (1.5).

Although by using Jastrow functions one significantly improves the SCH phonon spectrum, some properties of solid helium calculated with $f_J(r)$ (like the density at freezing [37] and the first moment of vibrations) are incorrect. For example, the first moment of vibrations $< u >$ comes out not zero [1], because the functions $f_J(r)$ are not centered on lattice sites [1].

1.3 Renormalization Phonon Theory

Horner [28] found a way to incorporate both the short-range correlations and anharmonicity in a systematic, consistent and unambiguous way. The method is based on the renormalization phonon theory. The fundamental quantity of the renormalization phonon theory is the phonon propagator, defined as:

$$d^{ij}_{\alpha\beta}(t) = - < x^i_\alpha(t) x^j_\beta(0) > + < x^i_\alpha(t) >< x^j_\beta(0) > \tag{1.21}$$

where x^i_α is the α component of position of an atom at a lattice point i and $t > 0$ is time. By using Fourier transformation and an analytic continuation to the complex plane, $\omega \to z$, the phonon propagator is represented as:

$$d_{\alpha\beta}(\mathbf{q}, z) = \sum_j \exp(-i\mathbf{q}\mathbf{R}_j) \int_0^{i\beta} d\tau \exp(i\tau z) d^{j0}_{\alpha\beta}(\tau), \tag{1.22}$$

where $\mathbf{q}$ is reciprocal wave-vector, $\mathbf{R}_j$ is lattice site of j atom, and without the loss of generality we set $i = 0$. The propagator $d_{\alpha\beta}(\mathbf{q}, z)$ is related to the spectral function, $A_{\alpha\beta}(\mathbf{q}, \omega)$, by

$$d_{\alpha\beta}(\mathbf{q}, z) = -i \int_{-\infty}^{+\infty} \frac{d\omega}{2\pi} \frac{A_{\alpha\beta}(\mathbf{q}, \omega)}{z - \omega} \tag{1.23}$$

The phonon shows up as peak in the spectral function. Thus according to Horner the knowledge of the $d^{ij}_{\alpha\beta}(t)$ is sufficient to obtain the phonon spectrum.

The phonon propagator can be calculated using the time-dependent Hamiltonian:

$$H = \sum_{i,\alpha} \frac{(p_\alpha^i)^2}{2m} + \sum_{i<j} v(x_{ij}) + \sum_{i,\alpha} U_\alpha^i(t) x_\alpha^i \tag{1.24}$$

where p_α^i is the α-component of particle momentum at a lattice site i' and x_{ij} is the distance between the i and j atoms. The $U_\alpha^i(t)$ is an external time-dependent force. The equation of motion for x_α^i is given by:

$$m\ddot{x}_\alpha^i = -\sum_{j:j\neq i} \nabla_\alpha^i v(x_{ij}) - U_\alpha^i(t) \tag{1.25}$$

Using the Hamiltonian (1.24) one constructs the generalized statistical sum (generating functional), Z:

$$Z = Tr\{T \exp\left(-i \int_0^{i\beta} dt H(t)\right)\} \tag{1.26}$$

where T is the time-ordering operator [38]. The one-point correlation function (the average position of the i atom) and two-point correlation functions (the phonon propagator) are derived from this generating functional according to:

$$d_\alpha^i(t) = \frac{\delta \ln Z}{\delta U_\alpha^i(t)} = -i < x_\alpha^i >, \tag{1.27}$$

and

$$d_{\alpha\beta}^{ij}(t) = \frac{\delta d_\alpha^i(t)}{\delta U_\beta^j(0)} = \frac{\delta^2 \ln Z}{\delta U_\alpha^i(t) \delta U_\beta^j(0)}, \tag{1.28}$$

where

$$d_{\alpha\beta}^{ij}(t) = - < x_\alpha^i(t) x_\beta^j(0) > + < x_\alpha^i(t) >< x_\beta^j(0) > \tag{1.29}$$

The quantum average of an operator, $\hat{O}(t)$, is defined as:

$$< \hat{O}(t) >= Z^{-1} Tr\{T\hat{O}(t) \exp\left(-i \int_0^{i\beta} dt H(t)\right)\} \tag{1.30}$$

The equation of motion for the one-phonon function, $d_\alpha^i(t)$, can be obtained by taking the quantum average of (1.25):

$$m\frac{\partial^2}{\partial t^2} d_\alpha^i = i \sum_{j:j\neq i} < \nabla_\alpha^i v(x_{ij}) > + i U_\alpha^i(t) = i\{K_\alpha^i + U_\alpha^i\} \tag{1.31}$$

where

$$K^i_\alpha = \sum_{j:j\neq i} < \nabla^i_\alpha v(x_{ij}) > \tag{1.32}$$

is the internal force acting on particle i. The equation of motion for the two-phonon correlation function can be found by taking a functional derivative of (1.31) with respect to the $U^j_\beta(0)$ (see the definition (1.28)):

$$m\frac{\partial^2}{\partial t^2} d^{ij}_{\alpha\beta}(t) = -\sum_{l,\gamma} \int_0^{i\beta} d\tau M^{il}_{\alpha\gamma}(t,\tau) d^{lj}_{\gamma\beta}(\tau) + i\delta_{ij}\delta_{\alpha\beta}\delta(t), \tag{1.33}$$

where

$$M^{il}_{\alpha\gamma}(t,\tau) = -i\frac{\delta K^i_\alpha(t)}{\delta d^l_\gamma(\tau)}, \tag{1.34}$$

is a generalized force constant, which describes change in the internal force K^i_α acting on the atom i, when the average position of the l atom has been changed by the external force. Thus the problem of evaluation of the phonon propagator is reduced to calculation of the generalized force constants. In principle, if K^i_α can be evaluated by computing the quantum average (1.32), then the $M^{ij}_{\alpha\beta}$ is found as a functional derivative of the K^i_α (1.34). In practice it is too difficult to compute analytically the average in (1.32), and Horner proposed to evaluate K^i_α using a pair correlation function, $g^{ij}_U(\mathbf{r}\mathbf{r}';t)$:

$$K^i_\alpha(t) = \sum_{j:j\neq i} \int d\mathbf{r} d\mathbf{r}' g^{ij}_U(\mathbf{r}\mathbf{r}';t) \nabla^i_\alpha v(|\mathbf{r}-\mathbf{r}'|) \tag{1.35}$$

The $g^{ij}_U(\mathbf{r}\mathbf{r}';t)$ must include the short range correlations strong anharmonicity typical for solid helium. Horner [28] noted that if $g^{ij}_U(\mathbf{r},\mathbf{r}';t)$ depends only on the distance between two atoms $g^{ij}_U(\mathbf{r},\mathbf{r}';t) = g^{ij}_U(|\mathbf{r}-\mathbf{r}'|;t)$ it can be written as:

$$g^{ij}_U(r;t) = f_0(r)\left(a_0 + a_1(r-R_{ij}) + a_2(r-R_{ij})^2\right) g_s(r;t) \tag{1.36}$$

where r and $R_{ij} = |\mathbf{R}_i - \mathbf{R}_j|$ is the distance between the atoms and the lattice sites i and j, respectively. The short range function $f_0(r)$ is obtained by solving

the Schrodinger equation for scattering of a pair of free particles. The $g_s(r;t)$ is a Gaussian (pair correlation function in a harmonic approximation):

$$g_s(r;t) = \sqrt{\frac{|D|}{\pi^3}} \exp\{-\sum_{\alpha\gamma\sigma}(\mathbf{r}-\mathbf{R}_{ij})_{\alpha\gamma} D^{ij}_{\gamma\sigma}(\mathbf{r}-\mathbf{R}_{ij})_{\sigma\alpha}\} \tag{1.37}$$

where the elements of the matrix $D^{ij}_{\alpha\beta}$ (width parameters) are defined as

$$D^{ij}_{\alpha\beta} = -\frac{1}{2}\left(d^{ii}_{\alpha\beta} + d^{jj}_{\alpha\beta} - d^{ij}_{\alpha\beta} - d^{ji}_{\alpha\beta}\right)^{-1} \tag{1.38}$$

The coefficients a_0, a_1 and a_2 are determined from the consistency requirements: they are chosen to normalize $g^{ij}_U(\mathbf{r};t)$, to set the first moment of vibration to zero ($< u >= 0$), and to make the second moment, $< u^2 >$, the same whether it is calculated with $g^{ij}_U(r;t)$ or with $g_s(r;t)$ [1].

With this ansatz for $g^{ij}_U(\mathbf{r};t)$ the phonon spectrum is calculated in the following way: firstly, starting with a harmonic approximation the parameters of the Gaussian matrix (1.38) are estimated and the internal force $K^i_\alpha(t)$ in (1.35) is evaluated. Then the generalized force constants are calculated according to (1.34), and $M^{ij}_{\alpha\beta}$ is Fourier transformed from $(\mathbf{r},t)$ to $(\mathbf{q},z)$.

Secondly, the two-point phonon propagator in the spectral representation is calculated:

$$d_{\alpha\beta}(\mathbf{q},z) = i\left\{mz^2 - M_{\alpha\beta}(\mathbf{q},z)\right\}^{-1} \tag{1.39}$$

and the spectral function $A_{\alpha\beta}(\mathbf{q},\omega)$ is derived from

$$d_{\alpha\beta}(\mathbf{q},z) = \int \frac{d\omega}{2\pi} \frac{A_{\alpha\beta}(\mathbf{q},\omega)}{z-\omega} \tag{1.40}$$

Using $A_{\alpha\beta}(\mathbf{q},\omega)$ Horner defined an "effective" non-physical frequency, $\Omega_{\mathbf{q}\lambda}$ via

$$\Omega_{\mathbf{q}\lambda} = \omega_{\mathbf{q}\lambda}\left(\int \frac{d\omega}{2\pi}[n_B(\omega)+1]\sum_{\alpha\beta}\epsilon_\alpha(\mathbf{q}\lambda)\epsilon_\beta(\mathbf{q}\lambda)A_{\alpha\beta}(\mathbf{q},\omega)\right)^{-1} \tag{1.41}$$

The Gaussian matrix $D^{ij}_{\alpha\beta}$ is corrected by using $\Omega_{\mathbf{q}\lambda}$:

$$D^{ij}_{\alpha\beta} = \sum_{\mathbf{q},\lambda} \frac{\hbar}{MN\Omega_{\mathbf{q}\lambda}} \epsilon_\alpha(\mathbf{q},\lambda)\epsilon_\beta(\mathbf{q},\lambda)(1-\exp(i\mathbf{q}\mathbf{R_{ij}}))\coth(\frac{\beta\hbar}{2}\Omega_{\mathbf{q}\lambda}) \tag{1.42}$$

and the pair correlation function is updated. The generalized force constants are recalculated again with $g^{ij}_U(\mathbf{r};t)$, and the procedure is repeated until consistency is achived. When convergence is achieved the physical phonon frequencies (for different polarizations λ) are obtained as positions of the maximum of the one-phonon spectral function, $A(\mathbf{q}\lambda;\omega)$

$$A(\mathbf{q}\lambda;\omega) = \sum_{\alpha\beta} \epsilon_\alpha(\mathbf{q}\lambda)\epsilon_\beta(\mathbf{q}\lambda)A_{\alpha\beta}(\mathbf{q},\omega) \tag{1.43}$$

The one-phonon spectral function calculated by Horner for different $\mathbf{q}$ of longitudinal phonons along the [111] direction is shown in Fig. 1.5. An interesting feature is the large weight at high frequencies. The secondary peaks are due to anharmonic admixture of two-phonon processes. Horner suggested that these peaks cannot be observed directly by inelastic neutron scattering since they are masked by multi-phonon excitations.

The longitudinal and transverse phonon branches calculated by Horner along the [001] and [011] directions are shown in Fig. 1.6 and Fig. 1.7, respectively. At low energies (below $\simeq$ 20 K) the agreement between the experimental data [9, 18, 19] and theoretical calculations is within 10%. This difference is due to omission of high-order terms (only the cubic term was included). At high energies the multiphonon excitations and interference terms become essential and as a result the calculated $\omega_\lambda(\mathbf{q})$ deviate considerably from the experimental data.

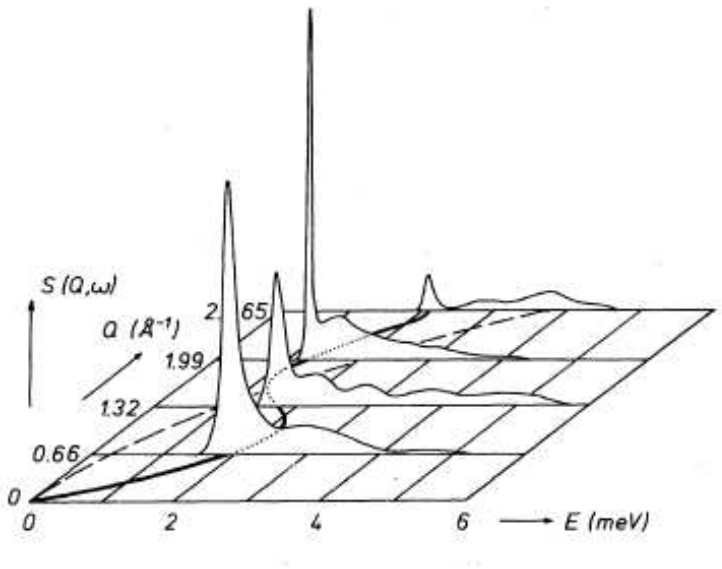

Figure 1.5: Dynamic structure function for different $\mathbf{q}$ along the [111] direction. Taken from [28].

1.4 Shadow Wave Functions

Reatto et al. [13] calculated the phonon spectrum of solid ^{4}He by using the Quantum Monte Carlo method based on Shadow Wave Functions (SWF). In the SWF for each real particle an additional shadow particle is introduced. The SWF wave function is written as:

$$\Psi_0([\mathbf{r}]) = \int ds_1 ... ds_N \Phi_P([\mathbf{r}]) K([\mathbf{r}],[\mathbf{s}]) \Phi_S([\mathbf{s}]) \tag{1.44}$$

where by vector $[\mathbf{s}] = \{\mathbf{s_1}, \mathbf{s_2}, \mathbf{s_3}....\mathbf{s_N}\}$ we denote the auxiliary shadow variables (one for each atom). The $\Phi_P([\mathbf{r}])$ contains the explicit part of inter-particle correlations, the kernel $K([\mathbf{r}],[\mathbf{s}])$ correlates real and shadow particles, and $\Phi_S([\mathbf{s}])$ is a Jastrow factor which correlates the shadow particles [13].

A longitudinal phonon, carrying momentum $\mathbf{q}$, can be described by associating

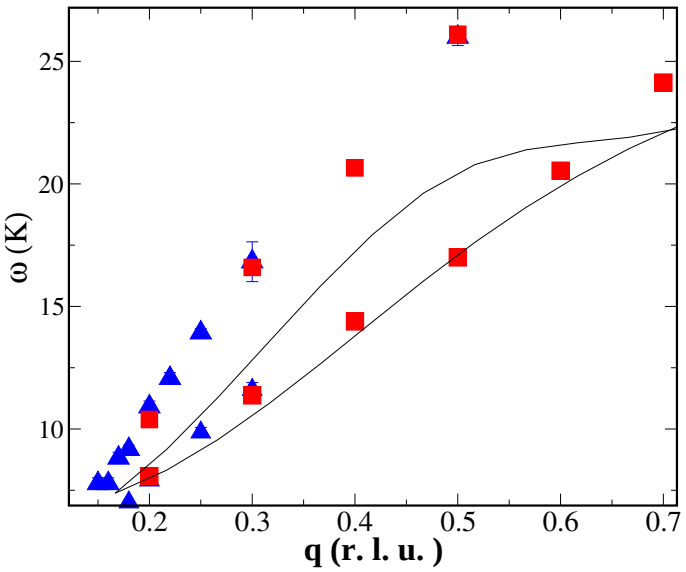

Figure 1.6: Dispersion curves (solid lines) for bcc ^{4}He at V = 21 cm^3/mol along the [001] direction calculated by Horner [28] . Experimental data from Osgood et al [18, 19] (triangles) and Markovitch [9] (squares).

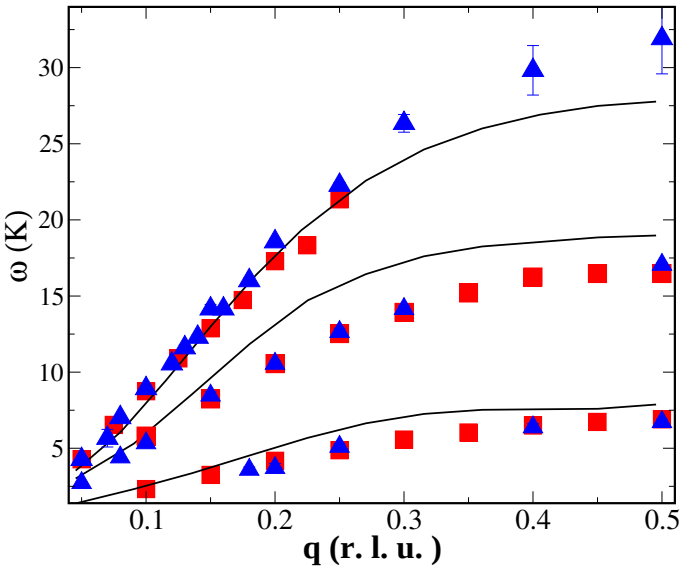

Figure 1.7: Dispersion curves (solid lines) for bcc ^{4}He at V = 21 cm^3/mol along the [011] direction calculated by Horner [28]. Experimental data from Osgood [18, 19] (triangles) and Markovitch [9] (squares).

an extra-shadow variable, S, with it in the SWF function [13]:

$$\Psi_{\mathbf{q}}([\mathbf{r}]) = \int ds_1 ... ds_N dS \Phi_P([\mathbf{r}]) K([\mathbf{r}], \{[\mathbf{s}], S\}) \Phi_S(\{[\mathbf{s}], S\}) \sum_j \exp\{i\mathbf{q}\mathbf{s}_j\} \qquad (1.45)$$

The longitudinal phonon branch at zero temepature was computed for each $\mathbf{q}$ by sampling total potential energy:

$$E(\mathbf{q}) - E(\mathbf{0}) = < \Psi_{\mathbf{q}}([\mathbf{r}]) | \hat{H} | \Psi_{\mathbf{q}}([\mathbf{r}]) > - < \Psi_0 | H | \Psi_0 > \qquad (1.46)$$

The results of the simulations are given in Fig. 1.8. The excitation spectrum of longitudinal phonons was found to be in good agreement with experiment.

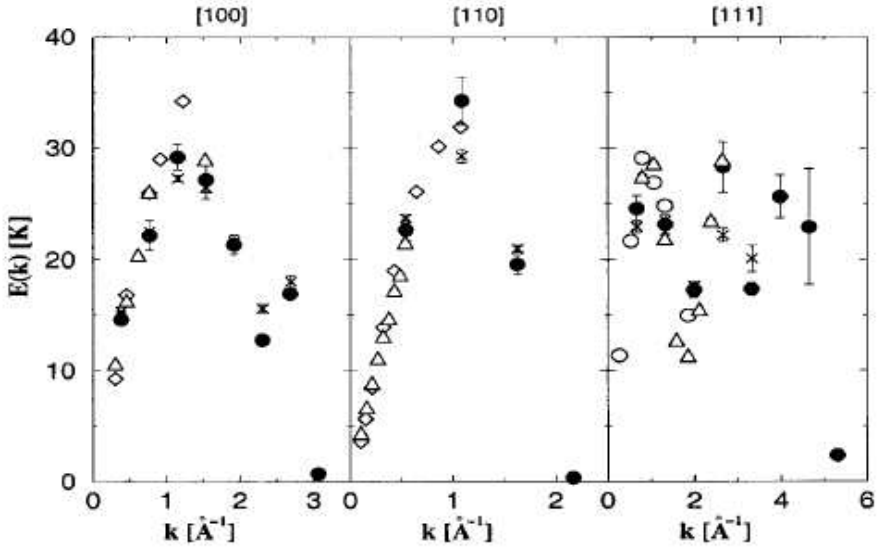

Figure 1.8: Longitudinal phonon frequencies in bcc solid ^{4}He computed at $\rho = 0.02898\ \dot{A}^{-3}$ along three different directions in a perfect bcc crystal (filled circles), in a bcc crystal with 0.8% concentration of vacancies (x), compared with experimental data (open circles and triangles). Taken from [13].

Despite of the substantial advancements of the SWF method (the most prominent example is its ability to reproduce the correct solid order, without imposing a solid symmetry on the trial wave function in advance), this technique has some limitations.

Firstly, the SWF method is a variational method: the Jastrow functions must be specified and their parameters optimized. The drawback of variation approach is that result depends on the variational ansatz used in calculations. As a consequence some properties of helium could not be obtained correctly by means the SWF method. For example, solid-liquid transition does not come out at experimental density in the SWF simulations. [2] Secondly, we study dynamics of solid helium in the bcc phase, which exists only in narrow finite temperature interval, while the SWF simulations are carried out at zero temperature. Therefore, we decided to use PIMC (the finite temperature Quantum Monte Carlo technique), described in detail in the next section.

Chapter 2

Model and Methods

In order to study the excitations in bcc solid helium ^{4}He at finite temperature we decided to use Path Integral Monte Carlo (PIMC)[2, 39] method. This method is based on Feynman's formulation of quantum mechanics in terms of path integrals [40]. It allows for simulations at finite temperatures, without constructing a trial wave functions and necessity for considering the individual excited states. The PIMC provides a direct statistical evaluation of quantum canonical averages. In addition dynamical properties can be extracted from PIMC simulations by means of the Maximum Entropy (MaxEnt) method. In our study the Universal Path Integral (UPI9CD PIMC) code of Ceperley [2] was adapted to calculate the phonon branches. The subject of this chapter is a short introduction to the PIMC and MaxEnt methods.

2.1 Path Integral Monte Carlo

At finite temperature, equilibrium properties of quantum systems can be calculated using the thermal density matrix, $\hat{\rho} = e^{-\beta \hat{H}}$. The expectation value of an observable

$\hat{O}$ at equilibrium:

$$< \hat{O} >= Z^{-1} Tr\left(\hat{\rho}\hat{O}\right) = Z^{-1} Tr\left(\hat{O}e^{-\beta\hat{H}}\right), \tag{2.1}$$

where $Z = \mathrm{Tr}(\mathrm{e}^{-\beta\hat{\mathrm{H}}})$ is the partition function.

The PIMC method is usually implemented in a position representation, $|[\mathbf{r}] >= |\mathbf{r_1}, \mathbf{r_2}, \mathbf{r_3}, \mathbf{r_4}, ... >$, where by vector $[\mathbf{r}]$ we denote the positions of all atoms. In this representation the density matrix is given by:

$$\rho([\mathbf{r}], [\mathbf{r'}]; \beta) =< [\mathbf{r}]|\mathbf{e}^{-\beta\hat{\mathbf{H}}}|[\mathbf{r'}] >, \tag{2.2}$$

where the elements of $\rho([\mathbf{r}], [\mathbf{r'}]; \beta)$ are non-negative and can be interpreted as probabilities. The $\rho([\mathbf{r}], [\mathbf{r'}]; \beta)$ contains the exponential of the Hamiltonian $\hat{H} = \hat{K} + \hat{V}$, where $\hat{V}$ is the potential energy and $\hat{K}$ is the kinetic energy. These operators are non-commutative, which makes them difficult to evaluate in (2.2). For small β (high temperature) one may approximate the density matrix as:

$$e^{-\beta(\hat{K}+\hat{V})} \simeq e^{-\beta\hat{K}} e^{-\beta\hat{V}} + O(\beta^2). \tag{2.3}$$

If β is large (low temperature), then β can be divided into many small segments, M, i.e. $\tau = \beta/M$.

The partition function, Z,

$$Z = \int d[\mathbf{r_0}] < [\mathbf{r_0}]| \exp(-\beta\hat{\mathbf{H}})|[\mathbf{r_0}] > \tag{2.4}$$

can be rewritten in the following form:

$$Z = \int d[\mathbf{r}_0] d[\mathbf{r}_1] ... d[\mathbf{r}_{M-1}] < d[\mathbf{r}_0]|-\tau\hat{H}|d[\mathbf{r}_1] >< d[\mathbf{r}_1]|-\tau\hat{H}|d[\mathbf{r}_2] > ... < d[\mathbf{r}_{M-1}]|-\tau\hat{H}|d[\mathbf{r}_0] >, \tag{2.5}$$

where the $M-1$ projection operators $\int d[\mathbf{r_i}]|[\mathbf{r_i}] >< [\mathbf{r_i}]| = \mathbf{1}$ are inserted, and the first element $|[\mathbf{r_0}] >$ and the last element $|[\mathbf{r_M}] >$ are equal as required by the trace

operator. In the short-time approximation the expression for $\rho([\mathbf{r_i}],[\mathbf{r_{i+1}}];\tau)$ is given by:

$$\rho([\mathbf{r_i}],[\mathbf{r_{i+1}}];\tau) =< [\mathbf{r_i}]|\mathbf{e}^{-\tau(\hat{\mathbf{K}}+\hat{\mathbf{V}})}|[\mathbf{r_{i+1}}] >\simeq (\mathbf{4}\pi\tau)^{-\mathbf{3N/2}} \exp\left(-\frac{|[\mathbf{r_i}]-[\mathbf{r_{i+1}}]|^{\mathbf{2}}}{\mathbf{4}\tau}\right) \exp\left(-\tau \mathbf{V}([\mathbf{r_i}])\right), \tag{2.6}$$

Substituting the result into (2.5) one obtains

$$Z = (2\pi\tau)^{-3MN/2} \int d[\mathbf{r}_0]d[\mathbf{r}_1]d[\mathbf{r}_2]....d[\mathbf{r}_{M-1}] \exp\left(-\tau \sum_{m=0}^{M-1}\left(\frac{[\mathbf{r}_{m+1}]-[\mathbf{r}_m]}{\tau}\right)^2 + V([\mathbf{r}_m])\right). \tag{2.7}$$

The integral (2.7) looks like a partition function of a classical ring polymer (see

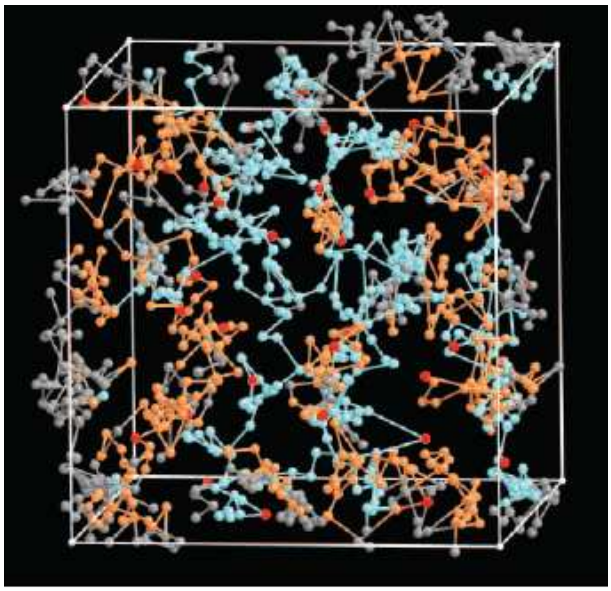

Figure 2.1: Snapshot of the path integral representation of atoms of helium in the superfluid regime, from [41].

Fig. 2.1), where the nearest beads are connected with elastic springs, while $V([\mathbf{r}])$ is an inter-atomic potential. Moving a quantum particle is equivalent to evolving this polymer. The only difference between the classical and quantum systems is that the potential interaction between these polymers occurs only at the same time slices

(beads), while in a real polymer all monomers interact with each other.(See Fig. 2.2). The expectation values are calculated by sampling the paths with the Monte Carlo

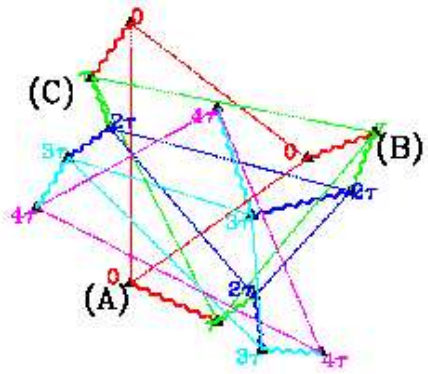

Figure 2.2: Cartoon of paths for 3 particles (A, B, C) with M=4, and $\tau = \beta/4$. The kinetic terms are represented by zig-zag lines and potential by dotted lines, which connect only beads of the polymers at the same time, from Bernu and Ceperley [39]

method. The simplest move is the translation of a whole chain. This move changes the potential energy of the system. If the relative position of the monomers is altered, then the kinetic energy is varied. Several algorithms have been proposed to sample the paths efficiently [2].

The Bose symmetry of the quantum particles increases significantly the complexity of the PIMC method. In order to take quantum statistics into account the density matrix is rewritten as:

$$\rho([\mathbf{r}],[\mathbf{r}'];\beta) = \frac{\mathbf{1}}{\mathbf{N!}} \sum_{\mathbf{P}} \rho(\mathbf{P}[\mathbf{r}],[\mathbf{r}'];\beta), \tag{2.8}$$

where P is the permutation operator ($P\psi(1,2) = \psi(2,1)$). The action of the permutation operator is equivalent to opening the ring polymers involved in the permutation and making a single polymer out of them.

The Path Integral Monte Carlo method for bosons is a non-perturbative numerical method, that allows, in principle, simulations of quantum systems without any

assumptions or uncontrollable approximations. The two body interatomic He-He potential is the only input for the PIMC simulations. In our simulations we used Aziz's potential [42] (See Fig. 2.3):

$$V(r) = \epsilon U(\frac{r}{r_m}) \tag{2.9}$$

$$U(x) = A\exp(-\alpha x) - \left(\frac{C_6}{x^6} + \frac{C_8}{x^8} + \frac{C_{10}}{x^{10}}\right) H(x) \tag{2.10}$$

and

$$H(x) = \begin{cases} \exp\left[-(D/x-1)^2\right] & x \le D \\ 1 & x \ge D \end{cases} \tag{2.11}$$

where $r_m = 2.9673\ \dot{A}$, $\epsilon = 10.8$ K, $A = 0.54485046\text{x}10^6$, α= 13.353384, C_6 =1.3732412, $C_8 = 0.4253785$, C_{10}= 0.1781, and D =1.241314.

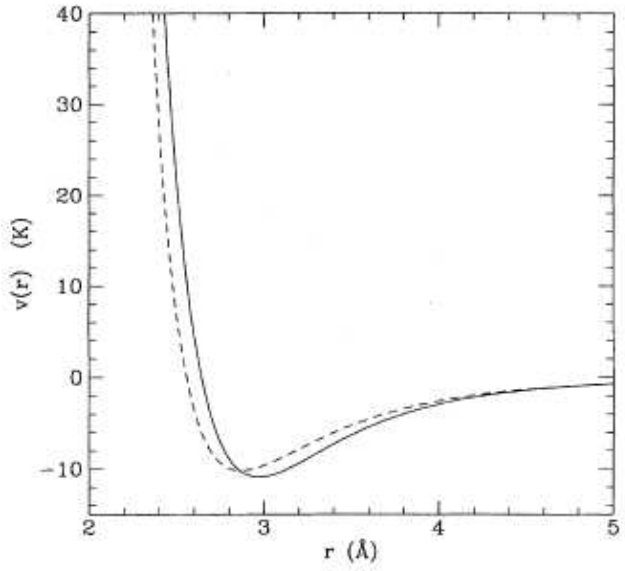

Figure 2.3: The semi-empirical He-He potentials : Aziz et al. [42] (solid line) versus Lennard-Jones potential (dashed line). Taken from [2].

The Aziz potential, which is superior to Lennard-Jones potential, was developed using both first-principle calculations and numerous experimental data. The main

feature of the potential is a strong hard-core repulsion at small distances and a weak attraction at larger distances.

The accuracy of the potential might be judged by comparison between the calculated and experimental data. For example, the experimental binding energy at zero pressure and temperature is -7.17 K, while QMC calculations, based on the Aziz potential, give a binding energy of -7.12 K [2]. This 1% error is due to the neglect of a weak repulsion coming from the overlaps of triplets of atoms. As the density is increased, contributions to the Aziz potential of explicit three-body and higher-order interactions become non-negligible. However, we study a low-density (bcc) phase of solid helium, where the many-body effects do not affect substantially any microscopic properties. The Aziz potential is close enough to the true potential [2], so that the physical properties can be predicted correctly by the PIMC.

2.2 Maximum Entropy Method

The object of this study is the phonon spectrum, which can be extracted from the dynamic structure factor, $S(\mathbf{Q},\omega)$. The definition of $S(\mathbf{Q},\omega)$ in terms of density fluctuations is

$$S(\mathbf{Q},\omega) = \frac{1}{2\pi n}\int_{-\infty}^{+\infty} dt e^{i\omega t} < \rho_{\mathbf{Q}}(t)\rho_{-\mathbf{Q}}(0) >, \tag{2.12}$$

where $\hbar\mathbf{Q}$ and $\hbar\omega$ are the momentum and energy (we take $\hbar = 1$), $\rho_{\mathbf{Q}}$ is the Fourier transform of the density of the solid, and $n = N/V$ is the number density. $S(\mathbf{Q},\omega)$ is usually expressed in terms of phonons, by writing $S(\mathbf{Q},\omega)$ as a sum of terms involving the excitation of a single phonon, $S_1(\mathbf{Q},\omega)$, a pair of phonons, $S_2(\mathbf{Q},\omega)$ and higher order terms which also include interference between different terms [1, 28]. In most of our simulations we calculated the $S_1(\mathbf{Q},\omega)$ term. Some calculations of $S(\mathbf{Q},\omega)$ were

also performed, and will be discussed below.

Taking the instantaneous position $\mathbf{r}(l,t)$ of atom l as the lattice point $\mathbf{R}_l$ plus a displacement $\mathbf{u}(l,t) = \mathbf{r}(l,t) - \mathbf{R}(l,t)$, we rewrite $S(\mathbf{Q},\omega)$ in terms of these displacements. The one-phonon contribution is then given by [1]

$$S_1(\mathbf{Q},\omega) = d^2(\mathbf{Q}) \sum_l e^{i\mathbf{Q}(\mathbf{R}_l - \mathbf{R}_0)} \left\langle [\mathbf{Q}\mathbf{u}(l,t)][\mathbf{Q}\mathbf{u}(l,0)] \right\rangle , \tag{2.13}$$

where $d(\mathbf{Q}) =< \exp(-\frac{1}{2}(\mathbf{u}\mathbf{Q})^2) >$ is the Debye-Waller factor. The displacement $\mathbf{u}(l,t)$ can be expressed using the phonon operators $A_{\mathbf{q},\lambda}(t)$ [66, 44]

$$\mathbf{u}(l,t) = \sum_{\mathbf{q},\lambda} A_{\mathbf{q},\lambda}(t) \exp\left(-i\mathbf{q}\mathbf{R_l}\right) \hat{\mathbf{e}}_\lambda, \tag{2.14}$$

where $\mathbf{q}$ is the phonon wave-vector, λ is the phonon branch index, and $\hat{e}_\lambda$ are polarization vectors, chosen along the directions [001],[011] and [111]. Using $A_{\mathbf{q},\lambda}(t)$, the one-phonon term $S_1(\mathbf{Q},\omega)$ for a specific phonon branch is rewritten as [1]

$$S_1 = \sum_{\mathbf{q},\lambda} \int_{-\infty}^{+\infty} < A_{\mathbf{q},\lambda}(t) A_{-\mathbf{q},\lambda}(0) > \Delta_{\mathbf{Q},\mathbf{q}-\mathbf{G}} d^2 [\mathbf{Q}\hat{\mathbf{e}}_\lambda]^2 e^{i\omega t} dt, \tag{2.15}$$

where $\Delta_{\mathbf{Q},\mathbf{q}-\mathbf{G}}$ is the delta function, and $\mathbf{G}$ is a reciprocal lattice vector. We use $\mathbf{Q}$, which lies inside the first Brillouin zone and parallel to one of e_λ. Therefore, $S_1(\mathbf{Q},\omega) = S_1(\mathbf{q},\omega)$, and $S_1(\mathbf{q},\omega)$ is given by

$$S_1 = \sum_\lambda S_{1,\lambda} = \sum_\lambda \int_{-\infty}^{+\infty} e^{i\omega t} F_{\mathbf{q},\lambda}(t) dt, \tag{2.16}$$

and

$$F_{\mathbf{q},\lambda}(t) = \int_{-\infty}^{+\infty} e^{-i\omega t} S_{1,\lambda}(\mathbf{q},\omega) d\omega \tag{2.17}$$

is the intermediate scattering function.

We cannot directly follow the dynamics of helium atoms in real time using the Quantum Monte Carlo method. However, we can extract information about the

dynamics by means of the analytical continuation of $F_{\mathbf{q},\lambda}(t)$ to the complex plane $t \rightarrow i\tau$. Using imaginary-time and the symmetry properties of $S_{1,\lambda}(\mathbf{q},\omega)$ [12] we obtain

$$F_{\mathbf{q},\lambda}(\tau) = \int_0^{+\infty} S_{1,\lambda}(\mathbf{q},\omega)\left(e^{-\omega\tau} + e^{-\omega(\beta-\tau)}\right) d\omega \tag{2.18}$$

where $F_{\mathbf{q},\lambda}(\tau)$ is the intermediate scattering function, and $\beta = 1/kT$.

In our simulations, we sampled the displacement $\mathbf{u}(l,\tau)$ for each "time-slice" τ of the l-th atom represented by a "ring polymer", and calculated $A_{\mathbf{q},\lambda}(\tau)$ by the performing spatial Fourier transformation

$$A_{\mathbf{q},\lambda}(\tau) = \sum_l \hat{\mathbf{e}}_\lambda \mathbf{u}(l,\tau)\exp\left(i\mathbf{q}\mathbf{R}_l\right) \tag{2.19}$$

Using (2.19), $F_{\mathbf{q}}$ is obtained as a quantum canonical average of the product of the phonon operator $< A_{\mathbf{q},\lambda}(\tau)A_{-\mathbf{q},\lambda}(0) >$ in equilibrium.

In order to calculate $S_{1,\lambda}(\mathbf{q},\omega)$ from Eq.(2.18), we need to perform an inverse Laplace transformation. Performing this inversion is a difficult numerical problem, [2, 45] because of the inevitable statistical uncertainty of noisy PIMC data. Even the smallest statistical errors in $F_{\mathbf{q},\lambda}(\tau)$ will be amplified by the inverse Laplace transform, and the noise rules out an unambiguous reconstruction of important features of the $S_{1,\lambda}(\mathbf{q},\omega)$. The best route to circumvent this problem is to apply the Maximum Entropy (MaxEnt) [45] method that makes the Laplace inversion better conditioned.

The MaxEnt method yields a dynamic scattering function, $S_{1,\lambda}(\mathbf{q},\omega)$ which satisfies Eq. (7) and at the same time maximizes the conditional probability imposed by our knowledge of the system. This can be done if some properties of $S_{1,\lambda}(\mathbf{q},\omega)$ are known. For example, the dynamic scattering factor is a non - negative function, and has certain asymptotic behavior at small and large ω. In the MaxEnt method the

probability to observe a given dynamic scattering function is given by

$$P(S_{1,\lambda}(\mathbf{Q},\omega)| < F_{\mathbf{q},\lambda}(\tau) >) \sim \exp\left(-\frac{1}{2}\chi^2 + \alpha S_{ent}\right) \tag{2.20}$$

where P is the probability to observe $S_{1,\lambda}(\mathbf{Q},\omega)$ for given set of sampled $< F_{\mathbf{q},\lambda}(\tau) >$, χ^2 is the likelihood, α is a parameter and S_{ent} is the entropy [45]. To simplify our notation, we use $S_1(\omega)$ below to denote by the one-phonon dynamic structure $S_{1,\lambda}(\mathbf{q},\omega)$ for a given $\mathbf{q}$ and λ, and omit the explicit dependence on $\mathbf{q}$ and λ. Similarly, we replace $F_{\mathbf{q},\lambda}(\tau)$ by F_τ. The likelihood χ^2 is given by

$$\chi^2 = \sum_{\tau,\tau',\omega} (K_{\tau',\omega}S_1(\omega) - < F_{\tau'} >)^T C^{-1}_{\tau',\tau}(K_{\tau,\omega}S_1(\omega) - < F_\tau >) \tag{2.21}$$

where the kernel $K_{\tau,\omega}$ is defined as

$$K_{\tau,\omega} = \exp(-\tau\omega) + \exp(-(\beta-\omega)\tau) \tag{2.22}$$

The covariance matrix, $C_{\tau,\tau'}$, describes the correlation between the different time slices τ for a given atom ("ring" polymer). This matrix is defined as

$$C_{\tau,\tau'} = < F_\tau F_{\tau'} > - < F_\tau >< F_{\tau'} >, \tag{2.23}$$

where $< F_\tau >$ is obtained as an average over all atoms at a given time slice τ. Because F_τ is periodic as one goes around the polymer[12], the summation on τ is done for $\tau = 1, M/2$, where M is the total number of time-slices in a "polymer ring". We remark here that in some QMC simulations only the diagonal elements of $C_{\tau,\tau'}$ are taken into account [45], but here we use all the elements, because the $< F_\tau >$ at different τ are correlated with each other.

Although χ^2 measures how closely any form of $S_1(\omega)$ approximates the solution of Eq. (7), one cannot determine $S_1(\omega)$ reliably from PIMC using χ^2 alone [2, 45].

The entropy term S_{ent} is added to χ^2 in order to make the reconstruction procedure better conditioned. The entropy term is given by

$$S_{ent}(\omega) = -\int_0^\infty d\omega \left(S_1(\omega) \ln \frac{S_1(\omega)}{m(\omega)} + S_1(\omega) - m(\omega) \right) \tag{2.24}$$

where $m(\omega)$ includes our prior knowledge about the properties of $S_1(\omega)$, examples of which were given above. The simplest choice of $S_1(\omega)$ is the flat model, in which $m(\omega)$=const for a selected range of frequencies and zero otherwise. We took a cutoff frequency corresponding to an energy of 100K. This flat model is used as an input for most of our simulations. In addition, we used a "self-consistent" model where the output of a previous MaxEnt reconstruction is used as input for the next MaxEnt reconstruction in an iterative fashion [2, 12]. The flat model is taken for the initial iteration. We also tried $m(\omega)$ with Gaussian and Lorentzian shape, with peaks given by the SCP theory and experiment. As explained below, the outcome is not very sensitive to the choice of $m(\omega)$ provided the PIMC data are of good quality.

Finally, we discuss the parameter α in (9). The magnitude of this parameter controls the relative weight of the PIMC data vs. the entropy term in the determination of $S_1(\omega_1)$. There are different strategies to obtain α. In our simulations we used both the "classical" MaxEnt method [45] and random walk sampling.[12] The "classical" MaxEnt method picks the best value of α, while random walk sampling calculates a distribution of α, $\pi(\alpha)$. Next, for each value of α we calculate $S_1(\omega)$. The final $S_1(\omega)$ is obtained as a weighted average over α. We found that when the collected PIMC data is of good quality, the distribution $\pi(\alpha)$ becomes sharply peaked and symmetric, and the phonon spectra obtained by means of "classical" MaxEnt and random walk are almost the same. Good quality data are characterized by an absence of correlation between sequential PIMC steps and by small statistical errors.

As an example, the dynamical structure factor for liquid ^{4}He at a temperature of $T = 1.2$ K calculated by Boninsegni et al. [12] is shown in Fig. 2.4. The MaxEnt method reproduces the overall shape of the dynamical structure factor, and gives accurate value for energy of excitations, but fails to resolve the double-peak structure observed experimentally. The method does not tell us how narrow the phonon - roton line is [2]. It is difficult to assign meaningful systematic error bars in this approach.

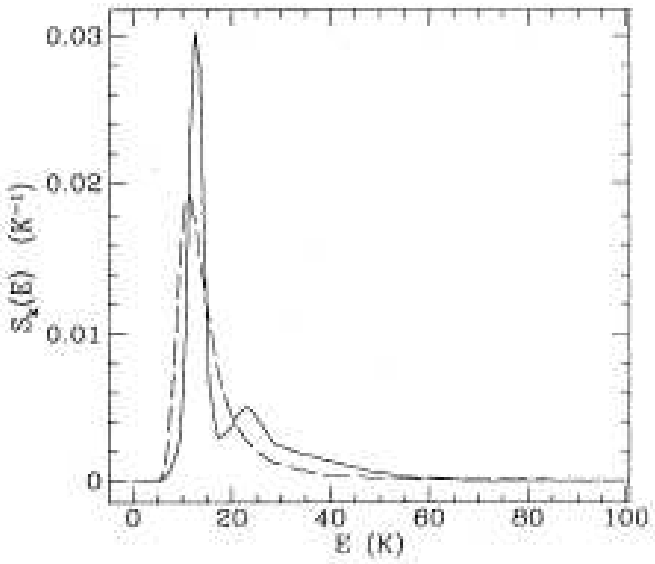

Figure 2.4: The dynamical structure factor for liquid ^{4}He at a temperature of 1.2 K and wavelength $\mathbf{q} = 0.76\ \dot{A}^{-1}$. Solid line, as measured by neutron scattering; dashed curve, as reconstructed from the PIMC imaginary-time response function by the maximum entropy method, from Ceperley [2]

.

Chapter 3

Results

At the beginning of the chapter we describe some computational details of the simulations: the initial conditions, the sample size and geometry, and the method used to estimate statistical errors. Then we present the results: the phonon spectra of ^{4}He, compared with experimental data, and the phonon spectra of ^{3}He, compared with theoretical calculations. The energy of formation of a vacancy in bcc solid ^{4}He obtained in our PIMC simulations is reported at the end of the chapter.

3.1 Computational details

In the simulations of ^{4}He samples containing between 128 and 432 atoms were used. This allowed us to calculate $S(\mathbf{q}, \omega)$ for values of q between 0.14 and 1 in relative lattice units (r.l.u.= $2\pi/a$, where $a = 4.12$ $\dot{A}$ is the lattice parameter). The number density was set to $\rho = 0.02854$ $(1/\dot{A}^3)$ (molar volume 21 cm^3) and the temperature was $T = 1.6$ K. Each helium atom was represented by a "ring"polymer with 64 time slices. A perfect bcc lattice was chosen as the initial configuration. We did not take

into account the effects of Bose statistics. This is a reasonable approximation for the solid phase of ^{4}He [46] are made possible the saving of a significant amount of CPU time.

The criterion determining the minimum number of sampled data points and number of Monte Carlo steps comes from the properties of the covariance matrix $C_{\tau,\tau'}$ (see 2.23). If there are not enough blocks of data the covariance matrix becomes pathological [45]. In addition, the MaxEnt method assumes that the distribution of the sampled F_τ is Gaussian. Therefore, we re-blocked [45] the sampled values of F_τ in order to reduce the correlations and to make the distribution as close as possible to a Gaussian with zero third and fourth moments). The number of collected blocks must be larger enough (large than the number of time slices in a "ring"polymer) to make re-blocking procedure reliable. We collected at least 300 blocks in each simulation run. We found that at least 10000 data points were required in order to obtain the 300 blocks. Each simulation run took about two weeks of 12 Pentium III PCs running in parallel.

Statistical errors were estimated by running the PIMC simulations 10 times, with different initial conditions (seed numbers) in each case. After each run, $S(\mathbf{q},\omega)$ was extracted using the MaxEnt method. The phonon energy for a given $\mathbf{q}$ was then calculated by averaging the positions of the peak of $S(\mathbf{q},\omega)$ over the set of the simulation runs. The error bars of each point shown in the figures below represent the standard deviation.

A typical example of the calculated dynamic structure factor is shown in Fig.3.11. The figure shows both the single phonon contribution $S_1(\mathbf{q},\omega)$ and the total $S(\mathbf{q},\omega)$ for a longitudinal phonon along the [001] direction. To illustrate the difference between $S_1(\mathbf{q},\omega)$ and $S(\mathbf{q},\omega)$, we chose to show the results for $\mathbf{q}$ close to the boundary

of the Brillouin zone. This difference is discussed below.

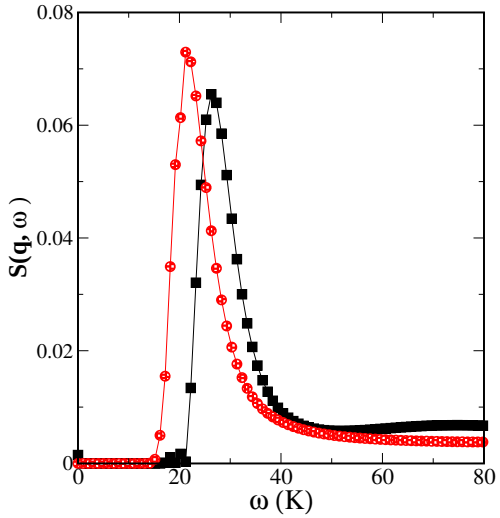

Figure 3.1: Longitudinal component of the dynamic structure factor, $S(\mathbf{q},\omega)$, for q = 0.83 r.l.u. along the [100] direction: single phonon contribution (circles), and total structure factor (squares). The solid lines guide the eye.

3.2 Phonon spectra of ^{4}He

The calculated longitudinal and transverse phonon spectra of solid ^{4}He in the bcc phase along the main crystal directions ([001], [111] and [011]) are shown in Figs. 3.12 - 3.17 (The numerical values are given in the Appendix A). We compare our results with the experimental data measured by inelastic neutron scattering from bcc ^{4}He with a molar volume of 21.1 cm^3 at T = 1.6 K by Osgood et al. [17, 18, 19], by Markovitch et al. [9] and by Peleg et al. [10].

As expected, the agreement between our simulations of $S_1(\mathbf{q},\omega)$ and experiment is very good at small $\mathbf{q}$, where one-phonon excitation is the most significant contribution to $S(\mathbf{q},\omega)$. As $\mathbf{q}$ increases, higher order processes, e.g. multi-phonon scattering and

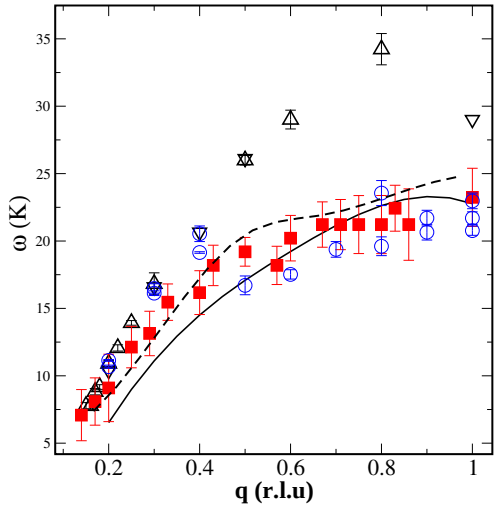

Figure 3.2: Calculated dispersion relation of the L[001] phonon branch (squares) using $S_1(\mathbf{q}, \omega)$. Experimental data are from [17, 19] (triangles up), from [9] (triangles down) and from [10] (circles). The error bars represent statistical uncertainty. For reference, phonon frequencies calculated by Glyde [1] (solid line) and Horner [28] (dashed line) are shown.

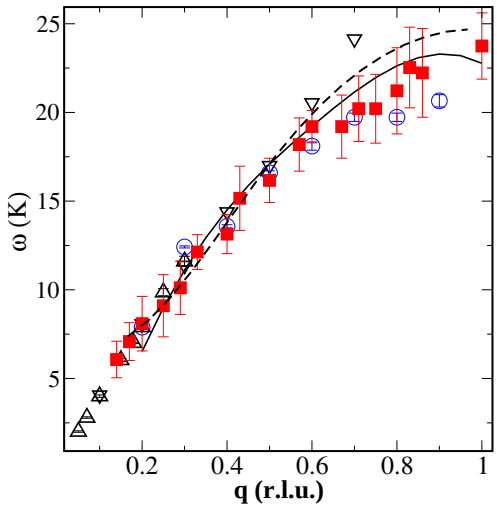

Figure 3.3: Calculated dispersion relation of the T[001] phonon branch (squares) using $S_1(\mathbf{q}, \omega)$. Experimental data are from [17, 19] (triangles up), from [9] (triangles down) and from [10] (circles). The error bars represent statistical uncertainty. For reference, phonon frequencies calculated by Glyde [1] (solid line) and Horner [28] (dashed line) are shown.

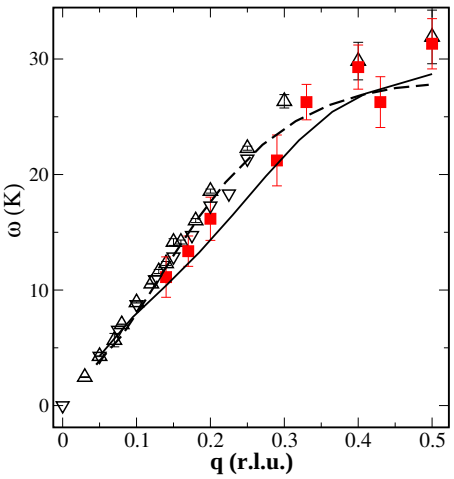

Figure 3.4: Calculated dispersion relation of the L[011] phonon branch (squares) using $S_1(\mathbf{q}, \omega)$. Experimental data are from [17, 19] (triangles up) and from [9] (triangles down). The error bars represent statistical uncertainty. For reference, phonon frequencies calculated by Glyde [1] (solid line) and Horner [28] (dashed line) are shown.

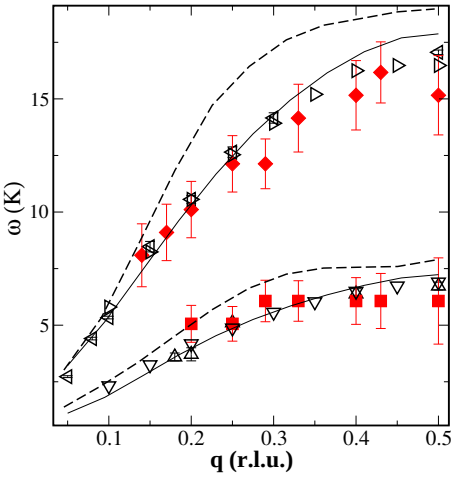

Figure 3.5: Calculated dispersion relations of transverse phonon branches along [011] using $S_1(\mathbf{q}, \omega)$. Calculated values are shown for the T_1 branch (squares) and T_2 branch (diamonds). Experimental data are from [17, 19] (T_1-triangles up, T_2-triangles left) and from [9] (T_1-triangles down, T_2-triangles right). The error bars represent statistical uncertainty. For reference, phonon frequencies calculated by Glyde [1] (solid line) and Horner [28] (dashed line) are shown.

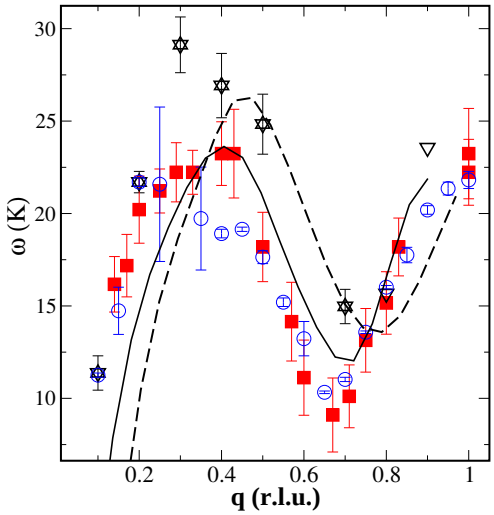

Figure 3.6: Calculated dispersion relation of the L[111] phonon branch (squares) using $S_1(\mathbf{q}, \omega)$. Experimental data are from [17, 19] (triangles up), from [9] (triangles down) and from [10] (circles). The error bars represent statistical uncertainty. For reference, phonon frequencies calculated by Glyde [1] (solid line) and Horner [28] (dashed line) are shown.

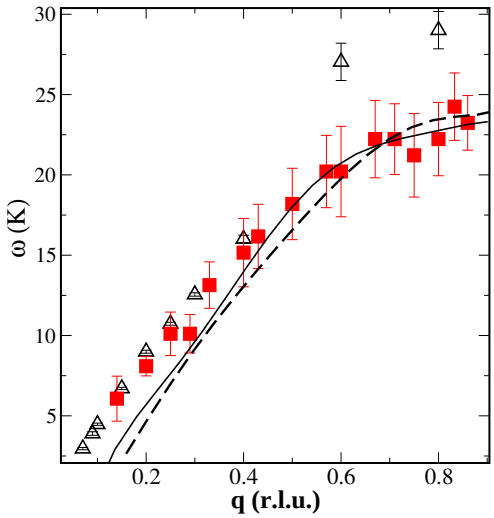

Figure 3.7: Calculated dispersion relation of the T[111] phonon branch (squares) using $S_1(\mathbf{q}, \omega)$. Experimental data are from [17, 19] (triangles up) and from [9] (triangles down). The error bars represent statistical uncertainty. For reference, phonon frequencies calculated by Glyde [1] (solid line) and Horner [28] (dashed line) are shown.

interference effects [1] become significant. Consequently, the position of the peak of in the $S_1(\mathbf{q},\omega)$ does not correspond to the position of the peak in the $S(\mathbf{q},\omega)$, and the phonon energies calculated from $S_1(\mathbf{q},\omega)$ are too low. The calculated values deviate from the experimental data, especially along [001] and [111].

In the case of longitudinal phonons, it is possible to calculate their energies using the total $S(\mathbf{q},\omega)$ obtained directly from Eq. (1) instead of just the single phonon contribution. The dispersion relations calculated with $S(\mathbf{q},\omega)$ are shown in Figs. 3.8 and 3.9. It is evident that using the total scattering function improves the agreement with experiment at large $\mathbf{q}$, especially for the [111] direction.

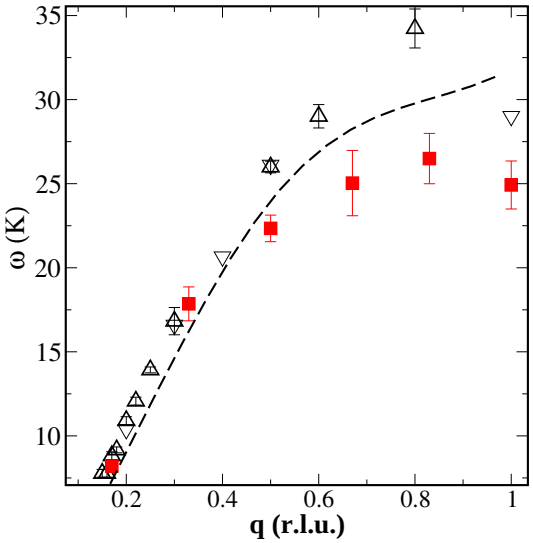

Figure 3.8: Calculated dispersion relation of the L[001] phonon branch (squares) using $S(\mathbf{q},\omega)$. Experimental data are from [17, 19] (triangles up) and from [9] (triangles down). The error bars represent statistical uncertainty. For reference, phonon frequencies calculated by Horner [28] (dashed line) are shown.

We point out that the calculated phonon branches $T_1[110]$, $T_2[110]$ and $L[110]$ show a good fit to the experimental data. Our results were obtained with the two body potential, which takes the He atoms to be point particles. Gov et al. [11]

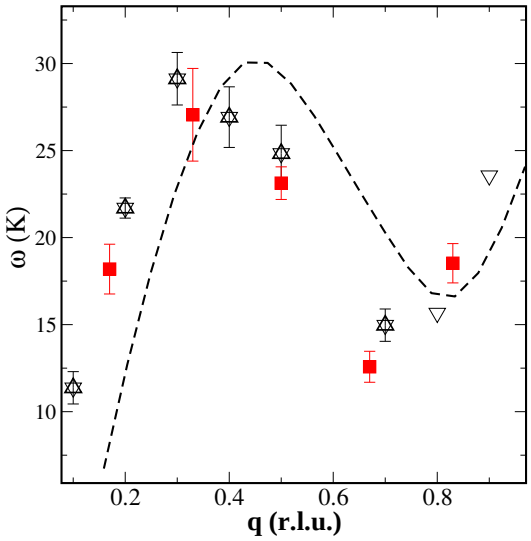

Figure 3.9: Calculated dispersion relation of the L[111] phonon branch (squares) using $S(\mathbf{q},\omega)$. Experimental data are from [17, 19] (triangles up) and from [9] (triangles down). The error bars represent statistical uncertainty.For reference, phonon frequencies calculated by Horner [28] (dashed line) are shown.

suggested that one needs to go beyond this approximation to obtain the $T_1[110]$ phonon branch in good agreement with experiment. Gov's approach also predicts the new excitation branch observed recently [8]. Although the calculated $T_1[110]$ branch is in agreement with experiment without any additional assumptions, we were not able to see the new excitation in our simulations. Experimentally, this excitation is about an order of magnitude less intense than a phonon. It is best observed in scattering experiments made with very small $\mathbf{q} \leq 0.1$ r.l.u. [9]. Both these factors make it very difficult to search for this excitation in simulations. Whether it can be found in this approach remains an open question.

In addition to experimental results, our simulations can also be compared with those of Galli and Reatto [13], who used the Shadow Wave Function approach to calculate the longitudinal phonon branches of bcc ^{4}He. As shown in Fig. 3.10, the

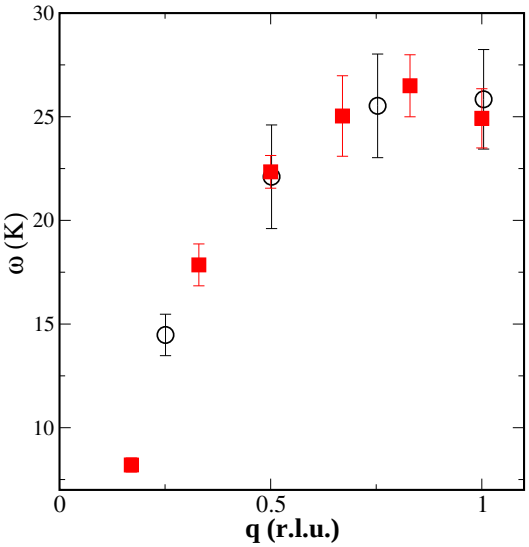

Figure 3.10: A comparison of dispersion relations of the L[001] phonon branch obtained in the present work using $S(\mathbf{q},\omega)$ (squares), with the same relation calculated by means of the Shadow Wave Function technique [13] (circles). The error bars represent statistical uncertainty.

overall agreement between these PIMC simulations and SWF results is good.

3.3 Phonon spectra of ^{3}He

In the simulations of ^{3}He we used samples containing between 128 and 432 atoms. Each atom was represented by a "ring" polymer with 64 time slices. $S(\mathbf{q},\omega)$ was calculated for values of q between 0.14 and 1 in relative lattice units (r.l.u.$= 2\pi/a$, where a is the lattice parameter). The number density was set to $\rho = 0.02801$ $(1/\mathring{A}^3)$ (molar volume 21.5 cm^3) and the temperature to T=1.6 K. This particular temperature was chosen to compare the phonon spectrum of ^{3}He with those of ^{4}He calculated at the same temperature [69]. A perfect bcc lattice was prepared for the initial configuration. The effects of Fermi statistics are not taken into account in our simulations,

which is a reasonable approximation for the solid phase at T=1.6 K.

As in case of ^{4}He, statistical errors were estimated by running the PIMC simulations at least 10 times, with different initial conditions in each case. After each run, $S(\mathbf{q},\omega)$ ($S_1(\mathbf{q},\omega)$) was extracted using the MaxEnt method [45]. The phonon energy for a given $\mathbf{q}$ was then calculated by averaging the positions of the peak of $S(\mathbf{q},\omega)$ over the set of the simulation runs. The error bars shown in the figures below represent the standard deviation. We collected at least 10000 data points in each simulation run and re-blocked the data [69] in blocks of 100-200 points [69].

A typical example of the calculated dynamic structure factor $S_1(\mathbf{q},\omega)$ along the [011] direction is shown in Fig.3.11. The figure shows both the longitudinal and transverse phonons. As seen in Fig.3.11 the two transverse phonons have narrow and almost symmetric line shapes, while the longitudinal phonon is quite broad and asymmetric. This asymmetry exhibits itself in the form of a relatively steep rise on the low-frequency side and a more gradual decrease on the high-frequency side. Similar form of the phonon spectral function was obtained by Koehler and Werthamer [23].

The calculated dispersion relations of longitudinal and transverse phonons, along the main crystal directions ([001], [111] and [011]), are shown in Figs. 3.12 - 3.17. (The numerical values are given in the Appendix).

For comparison, we plot the phonon branches calculated at T=0 K by Glyde and Khanna [3], by Koehler and Werthamer [23] (at molar volume V=21.5 cm^3) and Horner [36] (at molar volume V=24 cm^3). Koehler and Werthamer suggested that due to the asymmetry of the dynamic structure factor, the phonon frequency can be calculated either at the position of the maximum of $S(\mathbf{q},\omega)$ or as the mean of the two half-maxima [23]. Since we calculated the phonon spectra using the position of the maximum of $S(\mathbf{q},\omega)$ only these phonon frequencies were taken from Koehler and

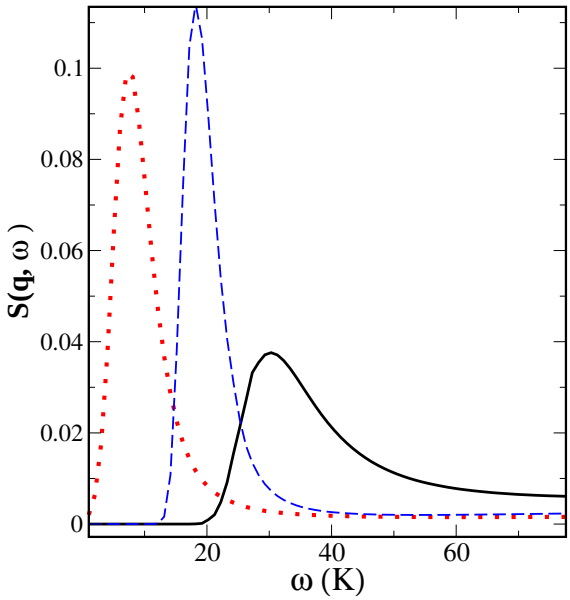

Figure 3.11: Longitudinal component (solid line) and transverse components (T_1 - dotted line, T_2 - dashed line) of the dynamic structure factor, $S_1(\mathbf{q}, \omega)$, for q = 0.4 r.l.u. along the [011] direction.

Werthamer [23].

In addition, we evaluated phonon frequencies in the long wavelength limit (q $\rightarrow$ 0) using the elastic moduli of bcc ^{3}He measured by Greywall[48] at molar volume V = 21.6 cm^3. We also made a fit to ^{4}He phonon branches calculated by the PIMC method [69], scaling them by square root of m(^{4}He)/m(^{3}He), the mass ratio of the isotopes, and plot in Figs. 3.12 - 3.17.

Surprisingly, we found that the results of ours simulations show good agreement with the theoretical calculation of Glyde and Khanne [3] (except the phonon branch T_1 [011] in Fig. 3.15). In addition, as can be seen from Figs. 3.12 - 3.17 the calculated phonon branches of ^{3}He coincide very closely with the scaled branches of ^{4}He (being practically on top of each other for longitudinal phonons). We conclude that, according to our simulations, the phonon frequencies of these two isotopes scale as

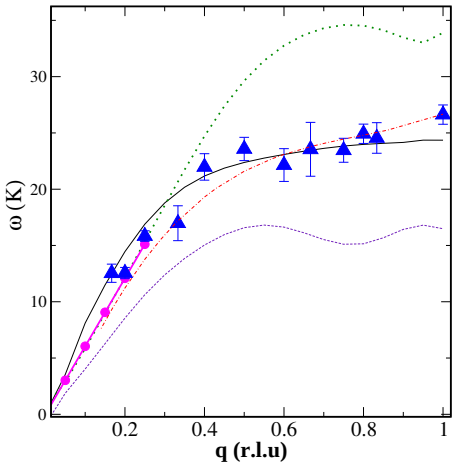

Figure 3.12: Calculated dispersion relation of the L[001] phonon branch (triangles) using $S_1(\mathbf{q},\omega)$. The error bars represent statistical uncertainty. For reference, phonon frequencies calculated by Glyde and Khanna [3] (solid line), Koehler and Werthamer [23] (dotted line) and Horner [36] (dashed line) are shown. The phonon spectrum at small q (circles) is estimated using elastic constants measured by Greywall [48], the dot-dashed line is the scaled single-phonon branch of ^{4}He.

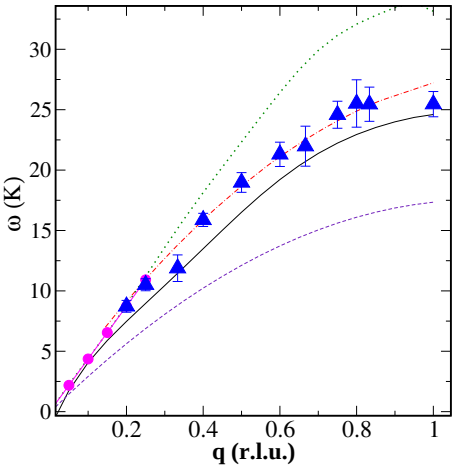

Figure 3.13: Calculated dispersion relation of the T[001] phonon branch (triangles) using $S_1(\mathbf{q},\omega)$. The error bars represent statistical uncertainty. For reference, phonon frequencies calculated by Glyde and Khanna [3] (solid line), Koehler and Werthamer [23] (dotted line) and Horner[36] (dashed line) are shown. The phonon spectrum at small q (circles) is estimated using elastic constants measured by Greywall [48], the dot-dashed line is the scaled single-phonon branch of ^{4}He.

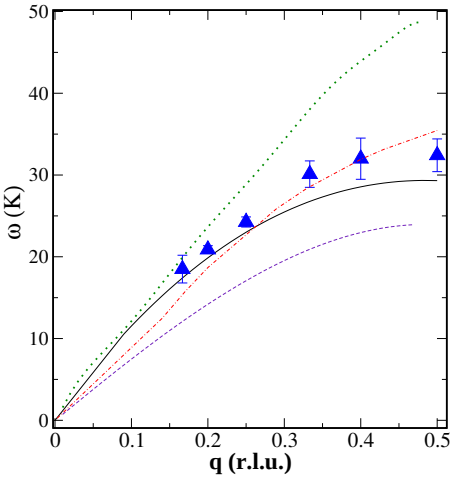

Figure 3.14: Calculated dispersion relation of the L[011] phonon branch (triangles) using $S_1(\mathbf{q},\omega)$. The error bars represent statistical uncertainty. For reference, phonon frequencies calculated by Glyde and Khanna [3] (solid line), Koehler and Werthamer [23] (dotted line) and Horner[36] (dashed line) are shown, the dot-dashed line is the scaled single-phonon branch of ^{4}He.

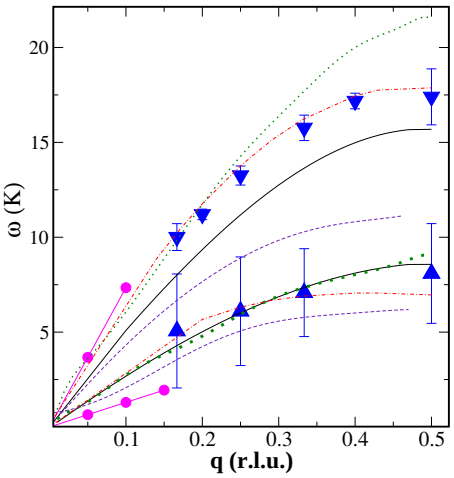

Figure 3.15: Calculated dispersion relations of transverse phonon branches along [011] using $S_1(\mathbf{q},\omega)$. Calculated values are shown for the T_1 branch (triangles down) and T_2 branch (triangles up). The error bars represent statistical uncertainty. For reference, phonon frequencies calculated by Glyde and Khanna [3] (solid line), Koehler and Werthamer [23](dotted line) and Horner [36] (dashed line) are shown. The phonon spectra at small q (circles) are estimated using elastic constants measured by Greywall [48], the dot-dashed line is the scaled phonon branch of ^{4}He.

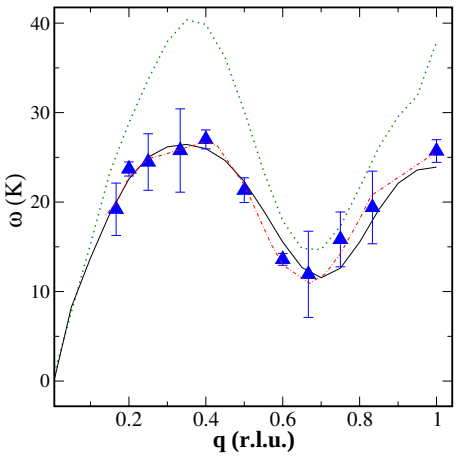

Figure 3.16: Calculated dispersion relation of the L[111] phonon branch (triangles) using $S_1(\mathbf{q},\omega)$. The error bars represent statistical uncertainty. For reference, phonon frequencies calculated by Glyde and Khanna [3] (solid line) along with frequencies calculated by Koehler and Werthamer [23](dotted line) are shown, the dot-dashed line is the scaled single-phonon branch of ^{4}He.

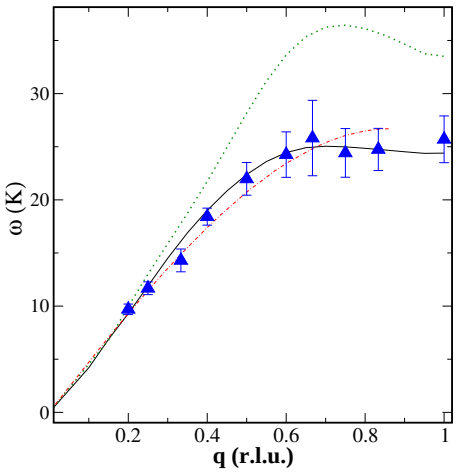

Figure 3.17: Calculated dispersion relation of the T[111] phonon branch (triangles) using $S_1(\mathbf{q},\omega)$. The error bars represent statistical uncertainty. For reference, phonon frequencies calculated by Glyde and Khanna [3] (solid line) along with frequencies calculated by Koehler and Werthamer [23](dotted line) are shown, the dot-dashed line is the scaled single-phonon branch of ^{4}He.

an inverse ratio of the square root of their atomic masses.

3.4 Vacancies

Recent experimental work [7] revived the interest in point defects, such as vacancies. In a quantum solid, defects such as vacancies on the atomic lattice are easily created and can be very mobile. They might even exist in finite concentrations at absolute zero. Although such zero-point vacancies have not been directly observed, they would be expected to condense into a coherent state at low temperatures.

It is therefore interesting to examine the influence of vacancies on the properties of the solid. We repeated our calculation of the phonon branches in the presence of 0.23% vacancies (1 atom of 432). Within the statistical error bars, we found no difference between the phonon energies with or without vacancies. Galli and Reatto [13] found that vacancies lower the energies of the phonons close to the boundary of the Brillouin zone. However, in their simulation they used a concentration of vacancies of 0.8%, so that the cumulative effect may be larger. We also calculated the vacancy formation energy, ΔE_v, according to Pederiva et al. [49]

$$\Delta E_v = (E(N-1,\rho) - E(N,\rho))(N-1), \tag{3.1}$$

where $E(N,\rho)$ is the total energy of N atoms. The energy $E(N,\rho))$ was calculated for a perfect crystal, while $E(N-1,\rho)$ was calculated after removing one atom. The density of two systems was kept the same by adjusting the lattice parameter. Values of ΔE_v calculated using the PIMC, Shadow Wave Function [47] and Shadow Path Integral Ground State [13] methods are summarized in Table 3.1. As will readily be observed in Table 3.1, the calculated ΔE_v depend on the sample size. We note that

different sample size corresponds to different concentration of vacancies, and therefore the values of ΔE_v do not need to be the same.

In addition, we calculated ΔE_v at constant volume, which is the condition usually realized in experiments rather than constant density. We obtained $\Delta E_v = 5.7 \pm 0.7$ K. The lower value arises since the repulsive part of the potential is weaker in a sample having lower density. There is no generally accepted experimental value [50] of ΔE_v. According to NMR studies [51, 52] the energy of vacancy formation in the bcc phase is $\Delta E_v = 6.5 \pm 0.2$ K, while X-ray studies[53] suggest that $\Delta E_v = 9 \pm 1$ K.

For classical solids, it is well known that a vacancy formation energy cannot be calculated accurately by means of a pair-potential, due to many-body contributions. The quantum effects in solid helium make this calculation even more complicated. Although, we could in principle add higher order terms to the Aziz potential, the absence of a generally accepted experimental value of the vacancy formation energy rules out the possibility of unambiguous estimation of the systematic error in ΔE_v due to a pair potential approximation.

It should also be noted, that the calculation of ΔE_v is a very CPU time consuming procedure. According to 3.1 the vacancy formation energy is estimated as a difference between the total energy of a perfect sample and a sample with a vacancy. The total energies of the perfect sample and the defected one are very close to each other. Therefore, in order to reduce statistical error and get a reliable result for ΔE_v our PIMC simulations must be run for a sufficiently long time. Statistical errors diminish relatively slow in MC simulations (as an inverse square root of the number of the sampled data). Given the limited computational resources in our disposal, the slow convergence of errorbars for the total energy in the PIMC runs prevented us from reliable estimation of ΔE_v for larger samples. As a result we cannot analyze the

dependence of the vacancy formation energy on of the sample size.

We comment here that the calculated values of ΔE_v are significantly smaller than 14 K, the energy of the new excitation observed by Markovitch et al.[8, 9]. Hence, this new excitation does not seem to be a simple vacancy.

Table 3.1: Calculated energy of formation of a vacancy, ΔE_v, for bcc solid ^{4}He. N is the number of atoms used in each of the simulations.

source	method	density $(1/A^3)$	N	ΔE_v (K)
this work	PIMC	0.02854	128	10.57 ± 0.38
this work	PIMC	0.02854	250	9.96 ± 0.89
ref.[47]	SWF	0.02854	128	8.08 ± 2.76
ref.[47]	SWF	0.02854	250	6.69 ± 3.86
ref.[13]	SWF	0.02898	128	8.9 ± 0.3
ref.[13]	SPIGS	0.02898	128	8.0 ± 1.3

Chapter 4

Melting under pressure: experiment

Phase diagrams of materials at high pressures and temperatures are of great interest due to their importance to geology, astrophysics and materials science. Fundamental questions about phase transformations, crystal structure and the nature of atomic bonding at high pressures can be answered using special experimental techniques. Experimental studies at high pressures are performed using the diamond anvil cell (DAC) [54] or the shock wave [55] technique which is the subject of this chapter.

4.1 Diamond anvil cell

A diamond anvil cell is a device used to exert extreme pressures on a material, almost as great as those found in the center of Earth ($P \simeq 200$ GPa, where 1 GPa = 10 000 bar = 9 870 atm). The DAC is based on the two cone-shaped diamonds squeezed together by a lever arm as shown in Fig. 4.1. A sample is placed between the diamonds; it is

surrounded by pressure transmitting medium and contained inside a hole in gasket. (See Fig. 4.1). In the melting experiments at high pressures the samples are small (typical dimensions are $\sim 10\mu$m thick and $\sim 50\mu$m in diameter), which could be a serious limitation of the method [59].

High pressures are generated by applying a force over a small area of the sample. Due to the transparency of the diamond the sample can be heated by a laser and examined in situ using diffraction techniques. The applied pressure and the sample temperature can be measured by spectral radiometry [59].

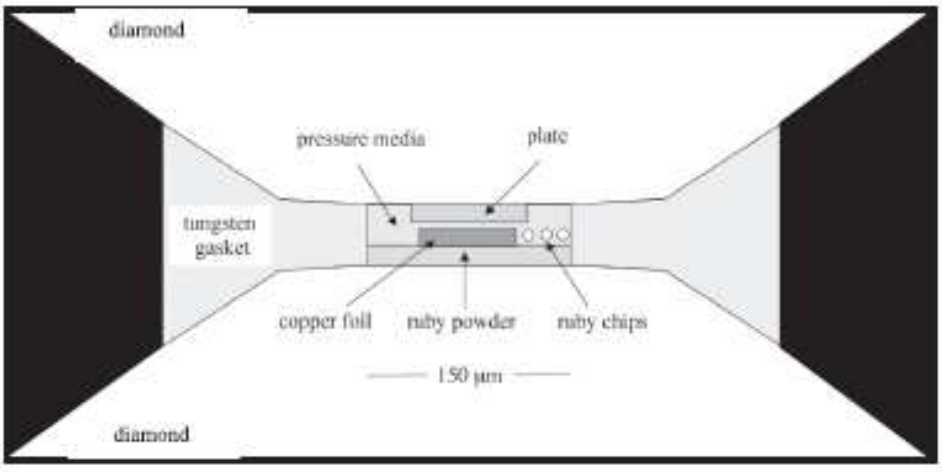

Figure 4.1: Schematic cross section of the DAC sample chamber. The sample (copper foil) is situated in a bed of ruby powder, and overlain by a pressure medium. Taken from [57].

In the melting experiments the phase transition is detected by optical methods. Visual observation of fluid flow, accompanied by an appearance of rapid and continuous motion in the interference pattern, is a common way to identify melting. However, at high pressures visual observation becomes ambiguous. Recently, x-ray diffraction has been applied to detect the phase transformation. The appearance of

diffusive scattering from the melt together with the simultaneous loss of crystalline diffraction signal are used to identify the melting transition.

4.2 Shock waves

When pressure is increased beyond ∼100 GPa DAC experiments become progressively more difficult [58], and above 200 GPa the only data available are from shock waves experiments [55]. In this method very high pressures (up to 600 GPa) can be achieved. These pressures occur inside the giant planets of our solar system, in the detonation of nuclear weapons, or when a large meteorite hits the Earth [60].

Shock wave is a strong pressure wave propagating through an elastic medium produced by phenomenon that create violent changes in pressure. The wave front of shock wave in which compression takes place, is a region of sharp change in stress, density, and temperature. The energy of the shock wave is expended to heat the medium in which it travels.

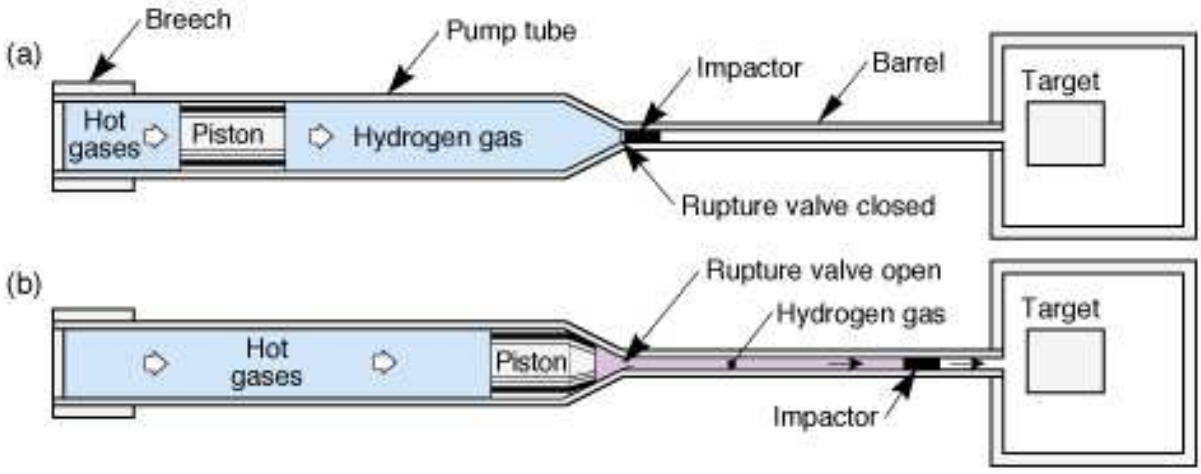

Figure 4.2: Livermore's two-stage gas gun. Taken from [60].

A typical experimental setup (two-stage gas gun) used in shock wave experiments is shown in Fig. 4.2. The gas gun consists of three major parts: a breech containing gunpowder, a pump tube filled with hydrogen, and a barrel for guiding a high-velocity projectile to the target. The gun is driven in two stages, first hot gases from the burning gunpowder drive a heavy piston down the pump tube, compressing hydrogen gas. Hydrogen is compressed before it breaks the rupture valve. Then hydrogen accelerates a projectile down the barrel to a high velocity. Once the projectile hits the target, the impact produces a high-pressure shock wave in a solid sample.

A stress pulse produced by shock waves divides the sample into two regions (see Fig. 4.3), which are an undisturbed region ahead of the shock wave front and a region of a new phase.

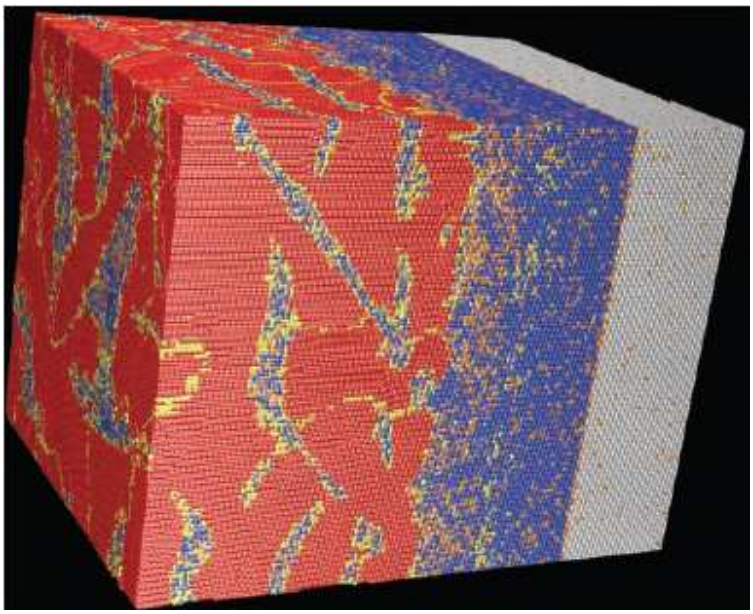

Figure 4.3: Shocked sample in the bcc phase of iron. Shock front propagates from left to right. Taken from [61].

Conservation of mass and momentum across the shock wave front leads to "jump

conditions" relating the initial and final states [55]. For an adiabatic system, the initial pressure, P_0, is linked with the final pressure, P, through:

$$P - P_0 = \frac{U_S U_P}{V_0} \tag{4.1}$$

where V_0 is the initial sample volume, P_0 is the initial pressure, and U_P and U_S is particle and shock wave velocity, respectively. According to (4.1) P in the transformed region, can be obtained by measuring U_S and U_P. U_S can be determined by detecting times of arrival of the wave at the detectors [55]. The same technique is adopted for U_P. The temperatures can be determined by analysis the light emitted from the shocked samples [55]. It should be noted, that the experimental error could be of the order of several hundred degrees kelvin.

The melting point is determined by finding a discontinuity in the slope of the U_S - U_P curve [55] or $P - T$ curve [75]. (See Fig. 4.4).

The interpretation of data obtained by this method is often questioned since the time scale of the shock wave experiments is very short [55]. In contrast to the static DAC, which operates slowly allowing careful observation of a material response to pressure, the shock experiments may last over in a millionth of a second or less. Thus if melting does not occur during the time available in a shock wave experiment, the solid can be superheated [55]. We found in the literature that there is no consensus concerning the mechanism of the melting transition in shock wave experiments. Some authors [56] claim that anomalous melting temperature in shock wave is due to non equilibrium. However, the time of measurements in these experiments is still much longer than the typical equilibration time after shock wave passage (which is order of picoseconds). We prefer to consider this melting as a bona fide equilibrium phase transition.

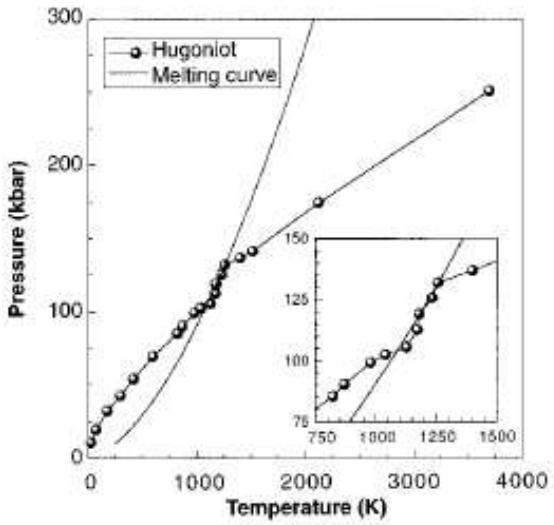

Figure 4.4: Pressure and temperature along the Hugoniot [55] curve compared with the melting curve for argon. Note the discontinuity in slope of the Hugoniot, which coincides with the melting point. Taken from [75].

Chapter 5

Melting under pressure: theory

Theories of melting can be separated into two classes. The first class treats the thermodynamic melting by taking both the solid and liquid phases into account [64, 5]. The second class considers only the solid phase and describes homogeneous or mechanical melting as a result of lattice instability and thermal generation of defects. [65, 66, 67, 68, 69]. According to the Born model of mechanical melting, a solid cannot be expanded above a critical volume, at which a 'rigidity catastrophe' occurs. This catastrophe is caused by the vanishing of the elastic shear modulus. In other words, the crystal melts once it loses its ability to resist shear. The application of these theories to the melting transition at finite pressures is outlined briefly in the following paragraphs.

5.1 Thermodynamic melting

First we consider the two-phase approach. According to thermodynamics the first-order melting transition occurs when the Gibbs free energies of solid, $G_s(P,T)$, and

liquid, $G_l(P,T)$ are equal: (See Fig. 5.1).

$$G_s(P,T_m) = G_l(P,T_m) \tag{5.1}$$

In addition, the Clausius-Clapeyron equation [64] can be derived from (5.1)

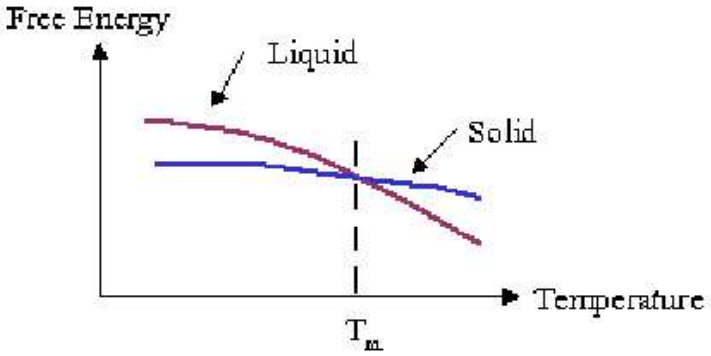

Figure 5.1: Variation of the Gibbs energy of a simple atomic substance near the melting point as a function of temperature at a given pressure.

$$\frac{dP(T_m)}{d\ln T} = \frac{T_m \Delta S}{\Delta V} \tag{5.2}$$

where ΔV and ΔS are the volume and entropy change on melting.

In 1929 Simon, relying on the Clausius-Clapeyron equation, proposed the first analytical expression for the melting curve of rare gas solids [64]. He assumed that the right hand side of (5.2) can be written as a linear function of pressure:

$$\frac{T_m \Delta S}{\Delta V} = c(P+a) \tag{5.3}$$

where c and a are constants. The constant c is related to the fraction f of the latent heat which goes to expand the solid on melting $c = -1/f$. The constant, a, is a volume derivative of the internal energy, U, at a fixed temperature: $a = -(\partial U/\partial V)_T$ [64]. Using this assumption Simon integrated (5.2) and obtained the following melting

curve:

$$T_m(P) = T_0\,(1 + \Delta P/a)^c \tag{5.4}$$

where $\Delta P = P - P_0$, and P_0 and T_0 are some reference pressure and temperature, usually taken at the triple point.

Kechin [70] suggested a more general form for the right hand side (5.2) and derived an unified equation for $T_m(P)$. The the right hand site of (5.2) was written as a rational function (fractional form) by expanding its numerator up to order M, and the denominator up to order L.

$$\frac{dP(T_m)}{d\ln T} = \frac{b_0 + b_1\Delta P + ...b_M(\Delta P)^M}{c_0 + c_1\Delta P + ...c_M(\Delta P)^L} \tag{5.5}$$

where $b_0, b_1, ..., b_L$ and $c_0, c_1, ..., c_M$ are constants. The integration of (5.5) with respect to pressure (for a particular choice of $M = L = 1$) leads to:

$$T_m = T_0(1 + \Delta P/a)^c \exp(-b\Delta P) \tag{5.6}$$

where the parameters a, b and c are identified in terms of the thermodynamic values of the solid and liquid phases [70]. This melting curve has the Simon rising function, and the damping factor $\exp(-b\Delta P)$ which decreases with pressure. This form predicts that each solid phase has a maximum (but no minimum) melting temperature at a positive or negative pressure. (See Fig. 5.2).

Although the unified equation (5.6) accurately reproduces the available experimental data, in order to predict $T_m(P)$ one has to calculate the Gibbs free energy of the solid and liquid phases. The Gibbs energy of simple (rare - gas) solids can be computed analytically by using quasi-harmonic lattice dynamics corrected by anharmonic terms. For the liquid phase, a modified hard-sphere variational perturbation theory can be applied. Young and Ross [74] calculated the $T_m(P)$ curve for rare-gas solids and hydrogen in good agreement with experiment.

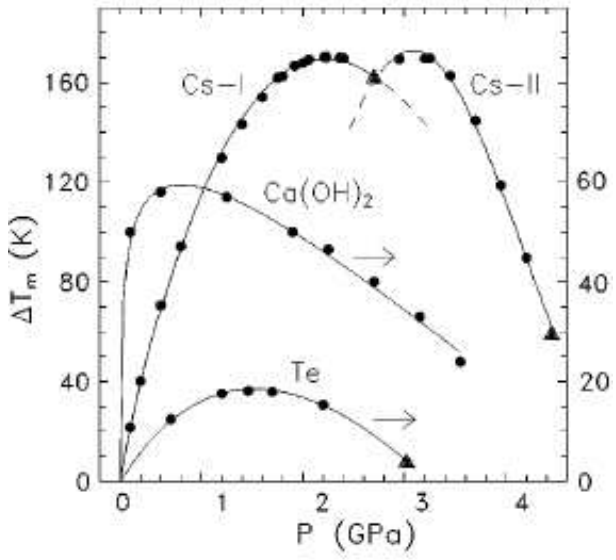

Figure 5.2: Melting curves for Cs, $Ca(OH)_2$ and Te . The solid lines are the fitting of the unified equation (5.6). Circles and triangles are experimental data. Taken from [70].

Alternatively, the Gibbs free energy can be obtained numerically by thermodynamic integration [77]. The calculations are carried out either by using effective inter-atomic potentials (constructed to reproduce experimental properties of materials) or by performing direct quantum mechanical (ab-initio) simulations [58]. In these simulations, the free energy $F(V,T)$ is commonly calculated and the Gibbs energy is derived from it by a Legendre transformation. By using the thermodynamic integration method one calculates the difference of the free energies $F_1 - F_0$ of the given system of interest (1) and the reference (0) system whose total energies are U_1 and U_0, respectively. $F_1 - F_0$ represents the reversible work done on switching the total energy from U_0 to U_1:

$$U_\lambda = (1-\lambda)U_0 + \lambda U_1 \tag{5.7}$$

where U_λ is a continuously variable total energy function. The work done in an

infinitesimal change $d\lambda$ is

$$dF =< dU_\lambda/d\lambda >_\lambda d\lambda =< U_1 - U_0 >_\lambda d\lambda \tag{5.8}$$

where the brackets denote a statistical thermal average for the system with U_λ potential. The difference of free energies is given by:

$$F_1 - F_0 = \int_0^1 < U_1 - U_0 >_\lambda d\lambda \tag{5.9}$$

$F_1 - F_0$ can be calculated by sampling $< U_1 - U_0 >_\lambda$ for a discrete set of λ and performing the integration numerically. The final F_1 is obtained by selecting the reference system with known F_0 (an ideal gas, a hard-sphere fluid, an Einstein crystal).

The most straightforward method to study the melting transition is to change the temperature and pressure and wait for phase transformation to occur [77] (this method is used in our simulations). For example, a system can be prepared in a crystalline phase, and then gradually heated up until it melts. In our simulations the temperature of the sample was raised by small steps. After each step the sample was equilibrated at a given temperature. An equilibrium was considered to be achieved when there was no significant variation of the total energy, pressure, and volume. The melting transition was indicated by a jump in the total energy and volume, simultaneous with the vanishing of the structure order parameter. (See details below). This method does not directly yield points on the melting curve, but provides upper or lower bounds, so a series of simulations is needed to locate the transition point.

Hysteresis near the first-order phase transition could be a potential problem for application of this method. It is well known that under special experimental conditions solids can be superheated. Superheating is may be considered as a reverse process of supercooling which is described by classical nucleation theory. This approach makes an attempt to study the kinetics limit of superheating.

Homogeneous nucleation is an onset of a phase transition in small regions [79] (liquid nuclei) inside a solid phase. The creation of a liquid nucleus implies the formation of an interface at the boundaries of the new phase. Some energy is expended to form this interface, based on the surface energy of each phase. In addition, as the result of the volume change of the solid (due to nucleation of liquid nuclei) the elastic strain energy density, ΔE, is changed. When a liquid spherical nucleus (with a radius r) appears in a solid matrix the Gibbs free energy, $\Delta G(r)$, is changed according to [80]

$$\Delta G = \frac{4\pi r^3}{3}(\Delta G_v + \Delta E) + 4\pi r^2 \gamma_{sl} \tag{5.10}$$

where $\Delta G_v = G_s - G_l$ and γ_{sl} is the solid/liquid interface energy (per unit area).

If a hypothetical liquid nucleus is too small, the energy that would be released by forming its volume is not enough to create its surface, and nucleation does not proceed. However, the nucleation barrier rising from the interface can be reduced to some extent by the interface disordering. The critical nucleus size can be denoted as by its radius, $r = r^*$, and it is when $r \geq r^*$ the nucleation proceeds. The critical radius is obtained by minimization of $\Delta G(r)$ with respect to r:

$$r^* = \frac{-2\gamma_{sl}}{3(\Delta G_v + \Delta E)} \tag{5.11}$$

As the phase transformation becomes more and more favorable, the formation of a given volume of nucleus frees enough energy to form an increasingly large surface, allowing progressively smaller nuclei to become viable. The rate of the nucleation, I, is given by

$$I \sim kT \exp(-\Delta G(r^*)/kT) \tag{5.12}$$

Eventually, thermal activation will provide enough energy to form stable nuclei. These can then grow until thermodynamic equilibrium is restored and the sample is melted.

Kinetics of homogeneous nucleation in superheated crystals were studied to derive a kinetic stability limit for the crystal lattice above its T_m [80]. It was found that at a critical temperature T_{mc} $1.2T_m$ a massive homogeneous nucleation of melting occurs in the superheated crystal. Such a homogeneous nucleation catastrophe, which occurs before other proposed (rigidity, volume, and entropy) catastrophes can intervene, provides us with a kinetic stability limit for superheated crystals [80].

Just as a simulated crystal with periodic boundary conditions can be overheated, our samples could be in principle superheated if nucleation of the liquid phase is suppressed (e.g. the shortest time of nucleation of the order of magnitude longer than the duration of our simulations).

One approach to avoid the hysteresis is by calculating Gibbs free energies of the solid and liquid phases. At the melting point the Gibbs free energies of both phases are equal and this must include bulk and surface and impurity (see below) shifted free energies. This is the essential point about the distinction between the melting of a crystal with a free surface and an infinite crystal, modeled with periodic boundary conditions. The difficulty is in calculating the Gibbs free energies of the different phases with the numerical method described above. We do not know how to choose the reference systems in both phases (with different boundary conditions specified at their surface) and calculate the corresponding free energies analytically. In additions we note there are a number of drawbacks in the Gibbs free energies technique: calculating the free energy requires a series of calculations, which takes up much computer time, and an error in the Gibbs free energy of 0.01 eV/atom may produce a corresponding error in the melting temperature of 100 K [78].

We recently have become aware of another possible approach for computation of melting curves, which is relied on the simulations of solid and liquid in coexistence.

The coexisting solid and liquid are simulated with the fixed total number of atoms, volume and internal energy. If the volume and energy are correctly chosen, the system equilibrates at a liquid-solid coexistence, and the average pressure and temperature give a point on the melting curve [78]. This method could be used to verify our simulations.

5.2 Dislocation mediated melting

In one-phase approach melting is a result of a thermal generation and proliferation of defects or mechanical instability of the crystalline lattice. One notable example of the one-phase approach to the melting transition at high pressures is the theory of dislocation mediated melting developed by Burakovsky et al. [62]. According to this theory pairs of dislocations are thermally excited at temperatures close to T_m. The presence of dislocations lowers the energy of creation of additional dislocations. This reduction leads to an avalanche of dislocations (melting transition) when the free energy of the crystal saturated with dislocations is equal to the free energy of the dislocation-free solid.

Using an approximation of perfectly screened non-interacting dislocations, which is valid in vicinity of T_m, Burakovsky et al. [62] found the following melting relation:

$$T_m = \frac{\lambda G v_{ws}}{8\pi \ln(z-1)} \ln\left(\frac{\alpha^2}{4b^2\rho(T_m)}\right) \tag{5.13}$$

where G is the shear modulus, v_{ws} is the volume of Wigner-Seitz cell, and z is coordination number of lattice. The Burgers vector denoted by b, while λ and α are constants which are different for screw and edge dislocations [63]. The dislocation density at T_m is estimated to be $\rho(T_m) = (0.61 \pm 0.2)b^{-2}$ according to available experimental data. The calculated T_m are in good agreement with the measured melting

temperatures at zero pressure (the accuracy of (5.13) is 17% for rare-gas solids).

In order to extend the melting relation (5.13) to high pressures Burakovsky et al. [63] assumed that only G and v_{ws} vary substantially with pressure:

$$\frac{G[P, T_m(P)]v_{ws}[P, T_m(P)]}{T_m(P)} = const \tag{5.14}$$

The pressure dependence of v_{ws} was obtained from the bulk modulus [63]. The shear modulus and bulk modulus were extrapolated to high pressures using only their values and first pressure derivative at room temperature and zero pressure:

$$G(P) = G_0 + G_0' \frac{P}{\eta^3} \tag{5.15}$$

where G_0 is the value at $P = 0$ and $G_0' = (dG/dP)_0$ is the first derivative of the shear modulus at zero pressure, and η is compressibility coefficient. The temperature dependence of the moduli was neglected. With these approximations Burakovsky et al. [63] established the $T_m(P)$ curve :

$$T_m(P) = T_m(0)\left(1 + \frac{B_0'}{B_0}P\right)^{-1/B_0'}\left[1 + \frac{G_0'}{G_0}P\left(1 + \frac{B_0'}{B_0}P\right)^{-1/3B_0'}\right] \tag{5.16}$$

where B_0 is the value at $P = 0$ and $B_0' = (dB/dP)_0$ is the first derivative of the bulk modulus at zero pressure. This equation (in its range of validity: $\mathrm{P} \leq 2\mathrm{B}_0$) is in reasonable agreement with the experimental data. (See Fig. 5.3).

Some molecular dynamics [71] and Monte Carlo [72, 73] simulations support the dislocation mediated melting theory. Cotterill [71] found that the free-volume distribution in a simulated Lennard-Jones liquid is heterogeneous. Chains of holes appear and persist for a long time. These chains were interpreted as dislocations remaining in the melt after the phase transition. Thermal excitations of line defects in a surface-free solid was studied by Gomez et al. [72, 73] by means of MC simulations. A model

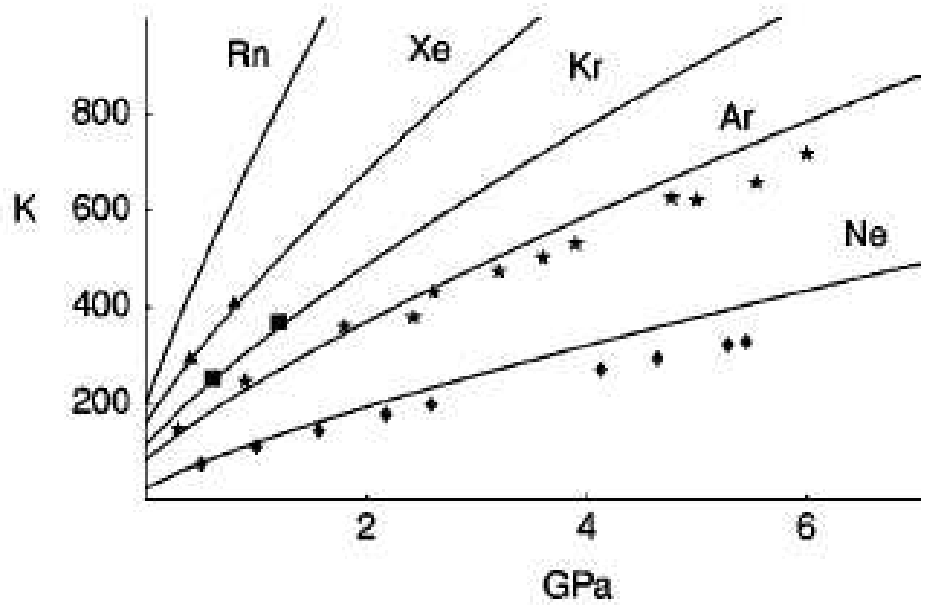

Figure 5.3: Melting curves for rare gas solids (solid lines) vs. experimental data (stars, boxes, triangles). Taken from [63].

system was represented by particles interacting through LJ 6-12 potential. Gomez et al. [72, 73] calculated the number of thermally excited defects, e.g. the number of particles with coordination number different from 12 for fcc lattice, as a function of temperature at different pressures. At low pressures when the solid is expanded thermally the number of defects increases with pressures. At high pressure when the solid is compressed the number of defects saturates. (See Fig. 5.4). Therefore, there is a crossover pressure, P_c, where volume expansion due to thermal effects is balanced by volume compression due to the external pressure. Above P_c, near T_m these defects become highly correlated and form very long dislocations that extend across the whole system.

It is well known that the compressibility and thermal expansion of the liquid state is normally higher than that of the solid state. It was conjectured a long time

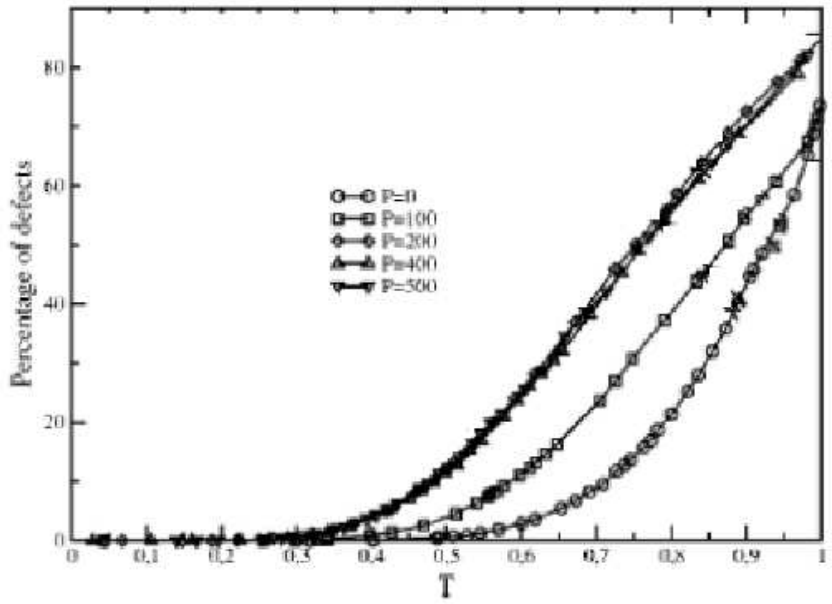

Figure 5.4: The percentage of defects as a function of the reduced temperature T/T_m for various pressures [73].

ago [64] that the volume difference ΔV as well as the entropy change ΔS on melting could gradually decrease as the applied pressure increases. If at some pressure and temperature both ΔV and ΔS become equal to zero, then critical melting where the change of phase is truly continuous could be attained. Gomez et al. [73] found that above the crossover pressure the volume jump on melting, ΔV, becomes pressure independent. (See Fig. 5.5) This observation probably rules out the possibility of continuous transition from a surface-free solid to a melt at high pressure (at least for rare gas solids).

Experimental evidence for thermal excitation of dislocations is too scarce [72] to conclude that dislocation-mediated melting theory is realistic. The premelting temperature region is very narrow and difficult to access experimentally. The results of Gomez et al. [73] indicate that experimental detection of dislocation mediated

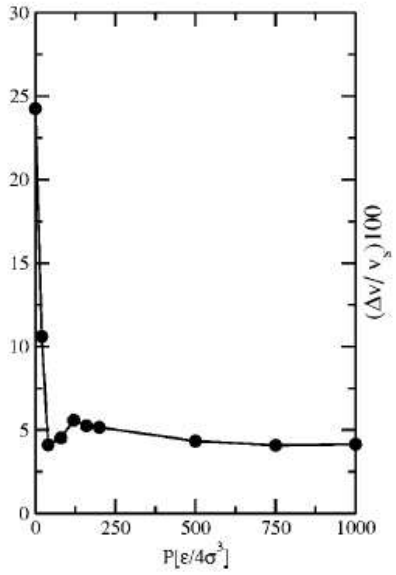

Figure 5.5: The percentage of volume jump ΔV as a function of pressure [73].

melting could be easier in high pressure studies of melting. We note that there is no consensus concerning the above discussion of dislocation-mediated melting theory, and it is beyond the scope of this thesis to discuss more details.

Chapter 6

Model and Method

In this chapter we describe the numerical method and the model used in our simulations of the melting transition at high pressure. Specifically, a model system of argon particles interacting via a pairwise potential was studied. First, we outline the algorithm employed in our simulations in the constant - NPT ensemble. Then we describe the geometry of the samples, specify the initial and boundary conditions and explain the procedure used to determine the melting point of argon at a given pressure.

6.1 Constant - NPT ensemble

In the laboratory, experimental conditions usually include a fixed pressure P, temperature T, and number of atoms N (constant-NPT ensemble). Therefore, we decided to perform simulations using this ensemble [77], which is also more suitable for the study of phase transitions than the constant-NVT ensemble. For example, in the NVT ensemble the system shows separation into two bulk phases of different density [77],

while keeping the mean density constant.

MC simulations in the constant-NPT ensemble are carried out using the Metropolis method as follows: first, we sample configurations of atoms at a fixed cell volume, then we attempt to change the cell volume. At the first stage each atom is displaced along a random direction. The total potential energy of the system before, U_o, and after, U_n, of this trial move is calculated. If the total energy decreases the trial move is accepted. Otherwise, we generate a random number $\eta \in (0,1)$ and calculate $\exp(-\beta(U_n - U_o))$. If $\eta < \exp(-\beta(U_n - U_o))$ the new configuration is accepted, otherwise it is rejected.

When the positions of all N atoms are sampled, we calculate the total potential energy, U_o, of the system and change the volume of the computational cell:

$$V_o \rightarrow V_n = V_o + \Delta V \tag{6.1}$$

The particle coordinates are rescaled according to V_n and new total energy, U_n, is computed. According to statistical mechanics [77] the probability density P_{NPT} that N atoms occupy a volume V at given P and T is:

$$P_{NPT}(V) \simeq \exp\left(-\beta(U + PV - N\beta^{-1}\ln V)\right) \tag{6.2}$$

From this follows that this volume change is accepted if $P_{NPT}(V_n) > P_{NPT}(V_o)$:

$$\ln(P_{NPT}(V_n)/P_{NPT}(V_o)) = \left(-\beta(U_n - U_o + P(V_n - V_o) - N\beta^{-1}\ln V_n/V_0)\right) > 0. \tag{6.3}$$

Otherwise, a random number $\eta \in (0,1)$ is compared with $P_{NPT}(V_n)/P_{NPT}(V_o)$. If $\eta < P_{NPT}(V_n)/P_{NPT}(V_o)$ the volume is changed, if not the attempt is rejected and the coordinates are rescaled back. In our simulations instead of changing the volume itself, the box length is varied. The box lenght L_x, L_y, and L_z are sampled independently

in order to take crystal anisotropy into account. The validity of the code was tested by direct calculation of the sample pressure using the virial theorem [77]:

$$P = \frac{NkT}{V} + \frac{1}{3V}\left\langle \sum_{i<j} \mathbf{f}_{ij}\mathbf{r}_{ij} \right\rangle \tag{6.4}$$

where $\mathbf{f}_{ij}$ is the force between particles i and j at the distance $\mathbf{r}_{ij}$. As shown in Fig. 6.1 the average pressure calculated is equal to the applied external pressure within statistical errors of MC method (which in this case is 0.2%). We also checked that pressure fluctuations are not too large to represent realistic bulk modulus, B. For this purpose we estimated the bulk modulus according to its definition

$$B = -V\left(\frac{\partial P}{\partial V}\right) \tag{6.5}$$

and by means of pressure fluctuations [85]:

$$B = \frac{k_b T}{< (P - < P >)^2 > V} \tag{6.6}$$

The calculated values do agree with each other.

6.2 Interatomic potential and sample geometry

The object of our study is the surface melting transition under external pressure. To simulate the external pressure we specified different boundary conditions at the surfaces: either hard walls or liquid neon were located at the each surface. We chose neon since it is a fluid under the conditions used and does not mix with argon. In the first case the argon was in contact with a rigid wall, represented by an infinite step function in the potential. In the second case we simulated solid argon in contact with a fluid neon layer. Our model crystal was a slab made of 44 atomic layers with two surfaces. (See Fig. 6.2). The argon atoms were subjected to periodic boundary

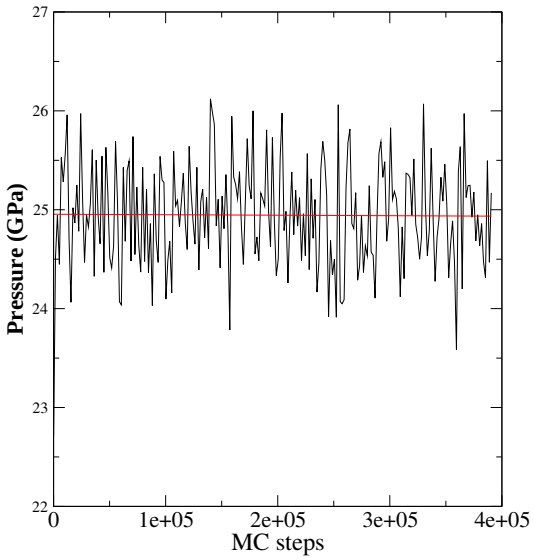

Figure 6.1: Variation of the pressure of a surface-free sample at T = 460 K. The applied pressure is $P_{ext} = 25$ GPa, the average pressure calculated with (6.4) is $< P_{int} >= 24.95 \pm 0.3$ GPa.

conditions only along the x and y directions (parallel to the free surface). We studied two different low-index surfaces: Ar(011) with 25 atoms per layer, and Ar(001) with 32 atoms per layer.

As a reference, we also simulated a surface-free solid sample with 864 atoms, by applying periodic boundary conditions in all directions. (See Fig. 6.3).

A system of argon particles interacting was simulated via a pairwise Lennard-Jones 6-12 potential:

$$U(r_{ij}) = 4\epsilon \left[\left(\frac{\sigma}{r_{ij}} \right)^{12} - \left(\frac{\sigma}{r_{ij}} \right)^{6} \right] \tag{6.7}$$

where r_{ij} is the distance between atoms i and j, ϵ and σ are characteristic energy and length scales, respectively. The LJ potential is truncated and shifted, such that

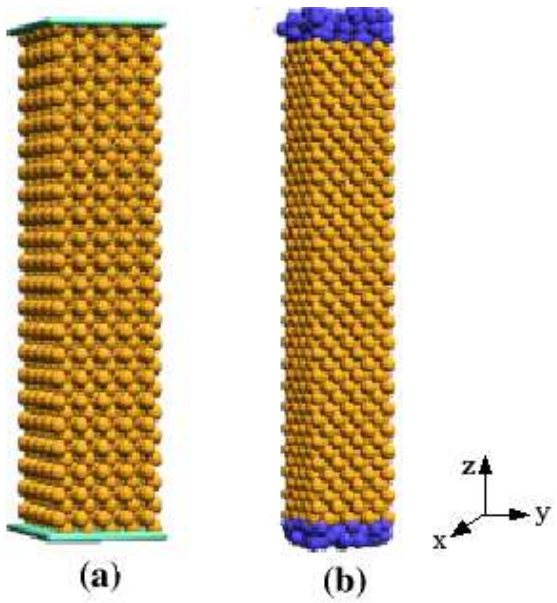

Figure 6.2: a) Snapshot of the Ar(001) sample bordered by hard walls at its top and bottom. (b) Ar(001) sample bordered by neon layers. Periodic boundary conditions were applied along x and y.

it and its first derivative vanish at the cutoff distance, r_c:

$$U(r_{ij}) = \begin{cases} 4\epsilon\left[\left(\frac{\sigma}{r_{ij}}\right)^{12} - \left(\frac{\sigma}{r_{ij}}\right)^{6}\right] + Ar_{ij} + B, & r_{ij} \leq r_c \\ 0, & r_{ij} > r_c \end{cases} \tag{6.8}$$

The cutoff distance was chosen to be $r_c = 2.1\sigma$. The values of the Ar-Ar parameters of the LJ potential are given in the Table 6.1. The interaction between the Ne-Ne and Ar-Ne atoms was also modeled using the LJ potential with parameters (see the Table 6.1) taken from [82]. As noted above, neon does not mix with argon under the conditions used in our simulations. The physical reason is that the energy gain due to the entropy of mixing turns out to be small in comparison with the potential energy due to interactions. We estimated the entropy of mixing (ΔS) by using the following formula [83]:

$$\Delta S = k_B(N_{ar}\log(N_{ar}/N) + N_{ne}\log(N_{ne}/N)) \tag{6.9}$$

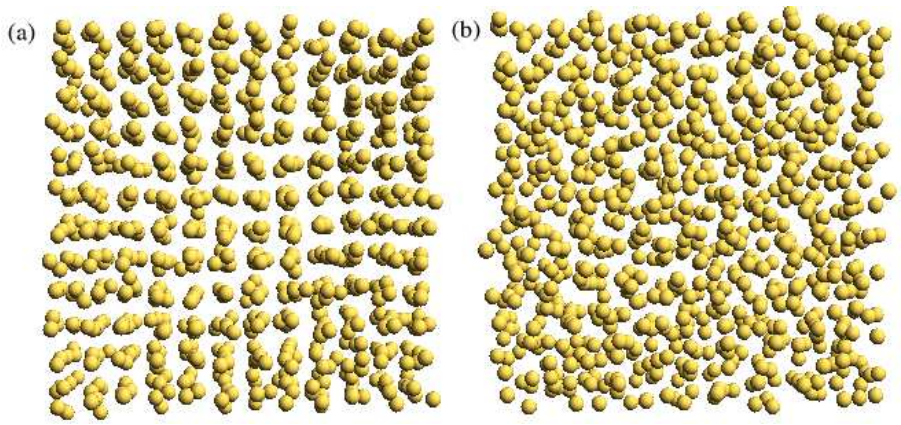

Figure 6.3: Snapshots of a surface-free (bulk) sample at pressure P=2.1 GPa and at $T_m = 3000$ K (a) Before the melting transition. (b) After the melting transition.

Table 6.1: Parameters of the LJ potential [82]

Type of atoms	ϵ (K)	σ (A)
Ar-Ar	0.0104	3.4
Ne-Ne	0.0031	2.74
Ar-Ne	0.0061959	3.43

where N_{ar} is the number of argon atoms, N_{ne} is the number of neon atoms, and $N = N_{ne} + N_{ar}$. The contribution of the entropy of mixing, $T\Delta S$, to the Gibbs energy was compared with average potential energy E_p taken from simulations at temperature close to T_m. (See Table 6.2). As can be seen from this table (Tab. 6.2) the entropy of mixing is small in comparison with the potential energy.

6.3 Efficiency and sample size

In order to speed up our simulations we applied various techniques (linked-cell list, Verlet list, and hybrid MC) developed for saving CPU time. We found that the

Table 6.2: Absolute value of entropy of mixing and average potential energy as a function of pressure at temperature close to T_m. The data is for the Ar(001) sample with N_{ar} = 1408 and N_{ne}= 216.

P (GPa)	T(K)	T$\|\Delta S\|$ (eV)	$\|E_p\|$(eV)
1.04	250	12.6	36.5
20.02	2020	110.8	710
30.01	2675	146.7	1017

Verlet list [77] is the most efficient method for energy and force calculations in our simulations. We also checked the effect of sample size on the calculated T_m. For this purpose a parallel code based on our serial MC program was developed. This code was written in C using MPI standard. The method of (1D) domain decomposition [81] was implemented. The sample was divided on equal length domains, with the largest length along the z-direction. (See Fig. 6.4).

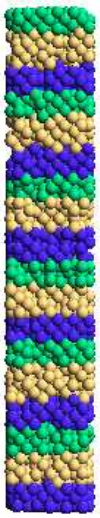

Figure 6.4: 1 D domain decomposition: each domain consists of the central subdomain (light-gray color), bordered by its upper (gray color) and lower (black color) subdomains. A sample with 3200 atoms.

Periodic boundary conditions were applied along the x and y directions. Each domain was divided into three subdomains: the central subdomain and two boundary subdomains. The length of the boundary subdomains was chosen to be equal to the cutoff of the LJ potential. During the simulation run each processor samples independently the particle positions in the central subdomain. The atomic configuration on the boundary subdomains is exchanged between the nearest neighbor processors (point-to-point communication). Collective communications were involved in the volume sampling and calculation of the total potential energy, order parameter and pressure.

By using samples with larger (or smaller) number of particles than stated above we found that T_m varies insignificantly with the system size (provide the number of atoms is still sufficiently large). The finite size effects are quite small for first-order transitions, due to the finite correlation length as the transition is approached. Our results are in line with those reported in the literature. [78, 72]

In addition we note that an another good check of convergence in calculation of T_m is to increase the area of the sample (by changing the X and Y sizes of the computational box) and to vary the distance between the surface of the argon slab and the hard walls (neon layers). The convergence tests for the samples with the different geometries, and the different boundary conditions at various pressures demand a significant amount of CPU time. Owing to this limitation we did not perform these calculations, but suggest they would be a useful extension in the future.

6.4 Initial conditions, equilibration, and melting

The initial conditions in our simulations differed according to the type of boundary. For the case of hard walls, the distance between the top surface layer of argon and the hard wall was set equal to the bulk interlayer distance. In the second case, the atoms of neon were initially arranged in a simple cubic lattice. Since the melting temperature of neon is lower than that of argon at all pressures [84], this boundary layer melted immediately and remained fluid at all temperatures at which simulations were made.

Each simulation was started at a low-temperature with a perfect fcc solid sample at a fixed pressure (P > 1GPa). The temperature of the sample was then gradually raised by 20K - 100K steps, (at low and high pressures respectively) and the sample was equilibrated. An equilibrium state was considered to be achieved when there was no significant variation (beyond the statistical fluctuations) of the total energy, pressure, volume and structure order parameter, η, defined through a spatial Fourier transform of the atomic density :

$$\eta = \left\langle \frac{1}{N^2} \left| \sum_j \exp\left(i\mathbf{k}\mathbf{r_j}\right) \right|^2 \right\rangle \tag{6.10}$$

where $\mathbf{r_j}$ denotes the coordinates of the atom j, $\mathbf{k} = (1/2\pi a)\,[0,0,1]$ is the reciprocal lattice vector along the [001] direction, a is the lattice parameter, and N is the number of atoms. The sum extends over all atoms in the sample, and the angular brackets denote statistical average.

The melting transition was indicated by a jump in the total energy and volume, simultaneous with the vanishing of the structure order parameter. (See Fig. 6.5 and 6.6) To improve the accuracy in the vicinity of T_m, we used smaller temperature steps of 10 K, and increased the number of MC steps by a factor of six. Throughout

this study, interactive visualization (the AViz program [86, 87]) was implemented to observe sample disorder and melting.(See Fig. 6.7)

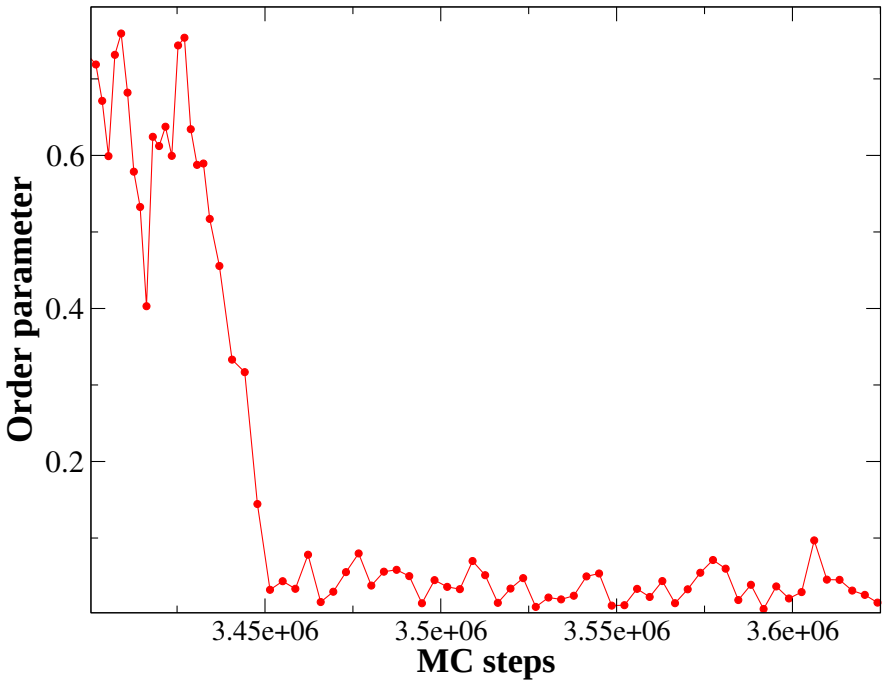

Figure 6.5: Structure order parameter at the melting transition. The Ar(001) sample bordered by neon layers at P = 27.24 GPa and T = 2600 K.

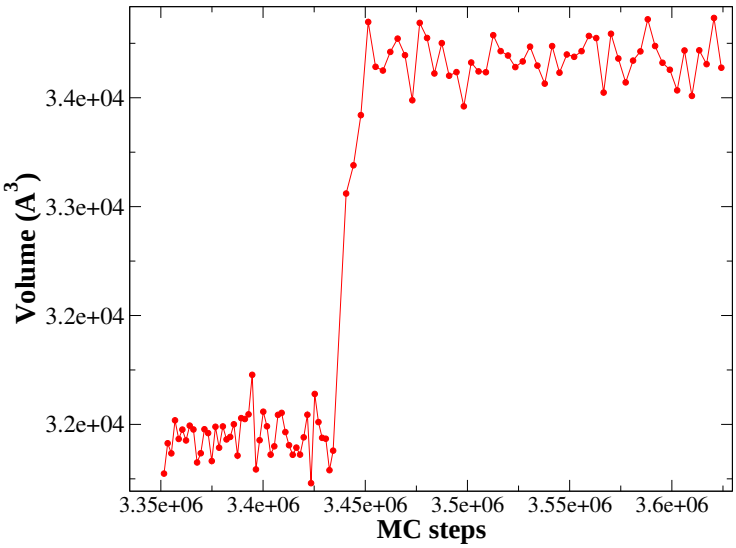

Figure 6.6: Volume jump at the melting transition. The Ar(001) sample bordered by neon layers at P = 27.24 GPa and T = 2600 K.

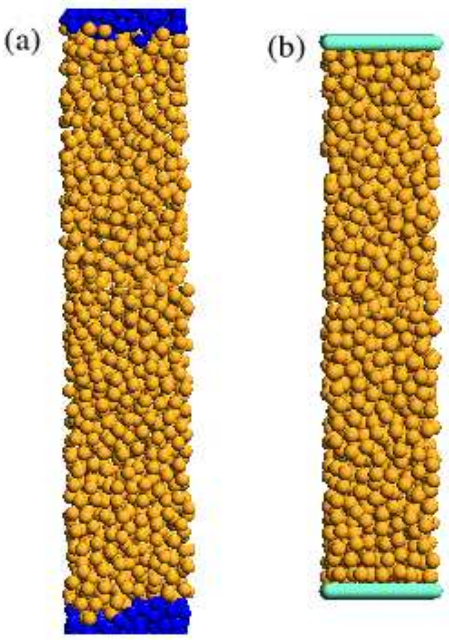

Figure 6.7: a) Snapshot of the Ar(001) sample bordered by neon layers at P = 27.24 GPa and T = 2600 K. b) Snapshot of the Ar(001) sample bordered by hard walls at T = 1360 K and P = 8.28 GPa.

Chapter 7

Result and Discussions

The melting curves calculated for the case of the hard wall are shown in Fig. 7.1 for both the Ar(001) and Ar(011) samples. (The numerical values are given in the Appendix B). For comparison, points showing T_m of the surface-free solid are also shown. These points are in very good agreement with a simulation (solid curve in Fig. 7.1) of a surface-free solid made by Gomez et al. [72]. It is seen that the argon sample bordered by hard walls melted at a temperature very close to that of a surface-free solid. The sample with the (011) surface melted at a slightly lower temperature than the sample with the (001) surface.

The melting curves calculated for the Ar bordered by fluid neon are shown in Fig 7.2 for the Ar(001) and Ar(011) samples. The curves are compared with those calculated for the surface-free solid. Within our resolution we did not observe a noticeable difference in T_m between samples with the (001) and the (011) surface.

A comparison of the melting curves for the samples with soft and rigid boundaries shows that the sample bordered by the neon layer melted at a systematically lower temperature than the sample with the hard walls. Another important difference,

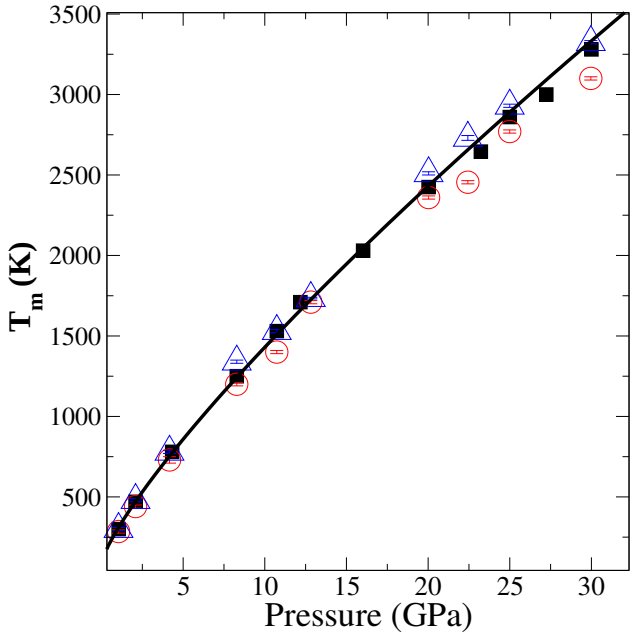

Figure 7.1: Melting temperature as a function of pressure for the samples with the hard walls: the Ar(001) sample (triangles) and the Ar(011) sample (circles). The solid black squares correspond to the (infinite) surface-free sample. The solid line is taken from [72]. Error bars are smaller than the size of the symbols.

shown in Fig. 7.3, is that premelting effects were absent in the sample with the hard walls, whereas in the case of the neon covered surface a gradual premelting was observed.

We interpret the above results as follows: the interactions with the hard wall seem to effectively inhibit the out-of-plane motion of the surface atoms. This result is shown in Fig. 7.4. In contrast, the in-plane and out-of-plane root mean square vibration amplitude in the sample bordered by fluid neon is approximately the same. Restriction of the out-of-plane motion suppresses thermal disordering of the surface. Absence of thermal disordering inhibits surface premelting and allows superheating up to the temperature at which crystal lattice becomes unstable. Consequently, superheating of argon bordered by hard walls is possible. The situation is analogous

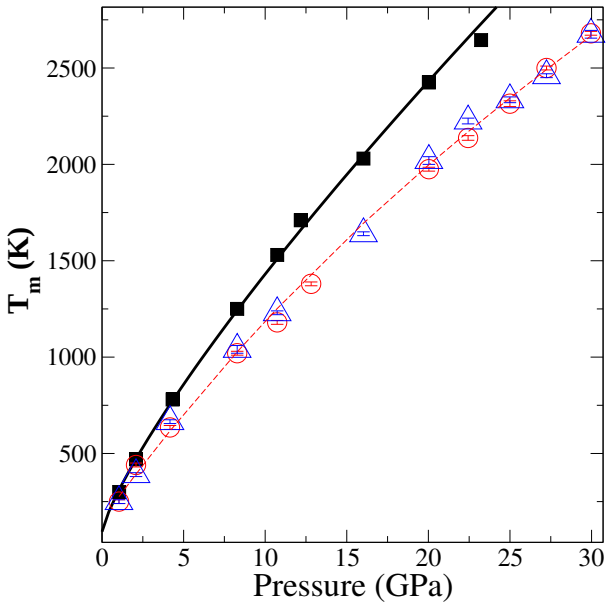

Figure 7.2: Melting temperature as a function of pressure for the samples with a neon layer at each surface: the Ar(001) sample (triangles) and the Ar(011) sample (circles). The black squares correspond to the (infinite) surface-free sample. The dotted line is drawn to guide the eye, and the solid line is taken from [72]. Error bars are smaller than the size of the symbols.

to the well-known experiment by Daeges et al. [88] in which superheating of silver coated with gold was demonstrated (gold has a higher T_m than silver).

It will be recalled that surface premelting can be regarded as a case of wetting, namely a wetting of the solid by its own melt. One may observe complete or incomplete wetting, depending on whether the quasiliquid thickness diverges or remains finite as $T \to T_m$. By the same analogy, the case of non-wetting corresponds to an absence of surface melting, e.g. the surface remains dry up to T_m. What makes the surface premelt or remain dry? If a single crystal is cleaved along it $\{hkp\}$ plane, where h, k, p are the crystallographic indices, then the surface free energy per unit of area $\gamma_{sv}^{\{hkp\}}$ is defined as the work needed to create a unit area of dry surface (the

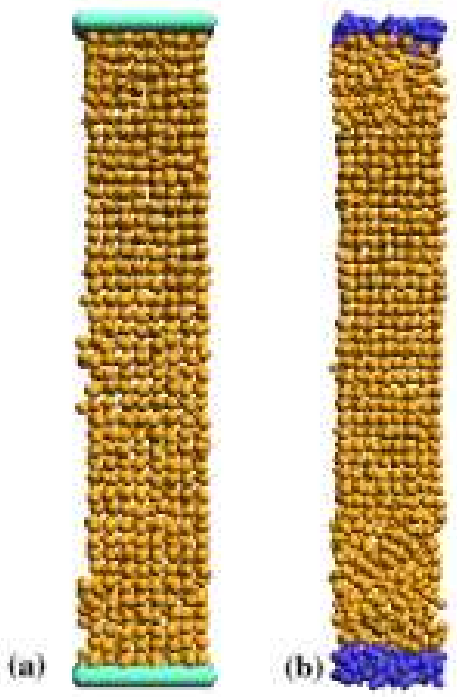

Figure 7.3: Snapshot of the Ar(001) slabs at P = 4.17 GPa: (a) a sample with hard walls at T = 740 K (T_m = 780 K). (b) a sample with neon layers at T = 625 K (T_m = 665 K). Note the presence of premelting near the surface of the Ar-Ne sample.

subscript 'sv' refers to the solid-vapor interface). On the other hand, the free energy of a surface that at T_m is covered with a thick melt layer, is given by $\gamma_{sl}^{\{hkp\}} + \gamma_{lv}$, where the indices 'sl' and 'sv' refer to the solid-liquid and liquid-vapor interfaces, respectively.

Surface premelting will only occur if there is a gain in the free energy, that is, if

$$\Delta\gamma^{\{hkl\}} \equiv \gamma_{sv}^{\{hkl\}} - \left(\gamma_{sl}^{\{hkl\}} + \gamma_{lv}\right) > 0 \tag{7.1}$$

However, if $\Delta\gamma^{\{hkp\}} < 0$, then the surface will remain dry up to T_m. The sign and magnitude of $\Delta\gamma^{\{hkp\}}$ depend not only on the material, but also on the surface orientation. In general the most open crystal faces are most likely to exhibit surface

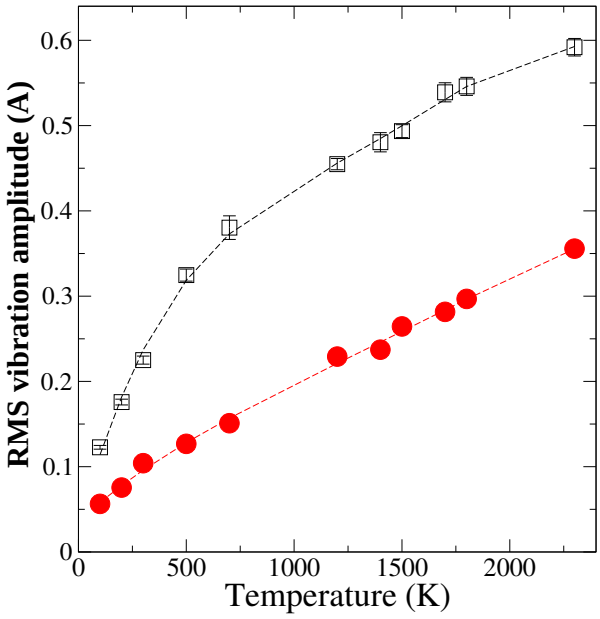

Figure 7.4: The depression of the out-of-plane atomic vibration amplitude (circles) relative to the in-plane vibration amplitude (squares), shown for the (001) sample with surface atoms bordered by a hard wall. The pressure is 20 GPa. The dotted lines guide the eye. Error bars are smaller than the size of the symbols.

melting. In our case solid-vapor interfaces are replaced by the hard walls or the liquid neon layers. Therefore, $\gamma_{sv}^{\{hkl\}}$, should be replaced by the corresponding surface energies which refer to solid argon - solid wall, $\gamma_{s_w}^{\{hkl\}}$, and solid argon - liquid neon, $\gamma_{s_ne}^{\{hkl\}}$ samples. While γ_{lv} should be replaced by γ_{lw} and γ_{lne}, respectively. According to the results of the simulations "non-wetting" condition corresponds to the case of where the sample was bordered by the hard walls $\Delta\gamma^{\{hkl\}} < 0$, while the sample bordered by the liquid layer undergoes a partial "wetting" transition $\Delta\gamma^{\{hkl\}} > 0$. One of possible extension of our study is to calculate the surface energies $\gamma_{s_ne}^{\{hkl\}}$, $\gamma_{s_w}^{\{hkl\}}$ as well as γ_{lw} and γ_{lne}. By using the surface energies one can estimate the total free energy of the surface covered with a melt layer and make perform thermodynamic analysis of the phase transition.

In our opinion, the conditions in the simulations with the hard walls are similar to those found in the shock wave experiments. The simulations can be related to the experiments in the following way: Typically, the part of the solid which is compressed during the propagation of the shock wave is much smaller than the size of the sample. Therefore, the instability occurs inside a region surrounded by a relatively cold material, which can act as a hard wall. Further support for this conjecture comes from the work of Kanel et. al. [89] who clearly observed superheating of aluminum single crystals with the shock wave technique. Another example where superheating is distinctly observed is in the case of compressed argon bubbles inside an aluminum matrix [90]. In this experiment the free surface of the solid was eliminated and as a result the solid was superheated. Therefore, the melting transition is closer to mechanical melting triggered by lattice instability.

On the other hand, in DAC experiments the material under study is usually surrounded by a hydraulic medium [4] so that it surface is in contact with a rare-gas or some other inert material. In addition the heating is usually done by a laser which heats mainly the surface. This situation is close to our simulations with the fluid neon layer. According to the results of the simulations, melting in this case is more like thermodynamic melting.

Before concluding we remark that the LJ (6,12) potential is not accurate enough at high pressures to allow quantitative comparison with experiment [91, 92, 75]. However, we believe that the generic nature of our results is still valid.

Chapter 8

Summary and Conclusions

In the first part of the research thesis we calculated the dynamic structure factor for solid helium in the bcc phase using PIMC simulations and the MaxEnt method. PIMC was applied to calculate the intermediate scattering function in the imaginary time from which the dynamic structure factor was inferred with the MaxEnt method. We extracted the longitudinal and transverse phonon branches from the one-phonon dynamic structure factor. At small wave-vectors $\mathbf{q}$, where the one-phonon excitation is the most significant contribution to the dynamic structure factor, the agreement between our simulations for ^{4}He and experiment is very good. At large $\mathbf{q}$, multi-phonon scattering and interference effects [1] become important. Consequently, the position of the peak of in the $S_1(\mathbf{q},\omega)$ does not correspond to the position of the peak in the $S(\mathbf{q},\omega)$, and the phonon energies calculated from $S_1(\mathbf{q},\omega)$ are too low. If $S(\mathbf{q},\omega)$ is used instead of $S_1(\mathbf{q},\omega)$, the agreement with experiment is significantly improved. We repeated the simulations in the presence of 0.23% of vacancies, and found no significant differences in the phonon dispersion relations. We also calculated the formation energy of a vacancy both at constant density and at a constant volume.

The calculation of the two-phonon and higher order phonon contribution to the dynamic structure is a more demanding task. With single phonon excitations, the energy of the peak of $S(\mathbf{q},\omega)$ is the quantity extracted from the calculations and compared with experiment. With multiphonon excitations, it is the detailed shape of $S(\mathbf{q},\omega)$ versus energy which one should compare with experimental data. Even though in principle there is no reason why it could not be done, in practice we found that the MaxEnt method does not resolve all the real structure observed experimentally. It is difficult to differentiate between "spurious structure", which is a result of noisy and incomplete PIMC data and "real structure" which represents atomic correlations. The MaxEnt favors the "smooth" Gaussian like spectral functions, and eliminates "spurious structure". Consequently, the asymmetric lineshape of multiphonon excitations and newly discovered excitations [8, 10] cannot be calculated with confidence using this method.

We also calculated the one-phonon dynamic structure factor for solid ^{3}He in the bcc phase. Both the longitudinal and transverse phonon branches were extracted from this structure factor. Good agreement between the calculated phonon spectra and the theoretical prediction of Glyde and Khanne [3] has been obtained. The results of our simulations show that the phonon frequencies of these two isotopes scale as an inverse ratio of the square root of their atomic masses.

In the second part of the research thesis we simulated the melting of a solid in the presence of two types of pressure transmitting medium at the sample boundaries. We found that with the soft medium (liquid neon layers) melting is closer to thermodynamic, nucleating at the surface, while with the rigid medium (hard walls) the solid exhibits superheating and melts via a lattice instability.

These results are related to high pressure melting experiments and appear to

be consistent with systematic differences that exist between shock wave and DAC measurements. We believe that the disparities between the results of measurements obtained with these two techniques at least to some degree originate in the different conditions at the solid-liquid interface. We suggest that results obtained with a DAC technique should be compared with thermodynamic theories, while shock wave results should be compared with theories based on a mechanical instability.

We want to stress again that it is not sufficient to use rigid walls with a much higher melting temperature to have this simulated effect of superheating. One needs this as *one necessary condition*, but the others are the degree of lattice misfit and more importantly, the nature of the rigid wall/solid argon interactions, whatever the materials, need be such that the liquid phase of the solid does not wet the hard wall/solid argon interface below the pressure shifted melting temperature. Hence, in principal it is possible to have thermodynamic (i.e. interfacially premelted) behavior in both configurations for a wide variety of experimental settings. Along these lines a necessary extension of our study would be to replace our structureless hard walls by more realistic solid walls.

It should be noted that in addition to the mechanism described above there may be additional effects which contribute to differences in the melting temperature determined by the two techniques. One possibility is the existence of a structural phase transition in that region of phase accessible in practice only to shock waves. Materials compressed using one of the two methods could in principle follow different paths in the P-T plane leading to an apparently large discrepancy in T_m [4]. The relative importance of these effects would depend on the material. In conclusion we note that the above discussion is one possible interpretation of the simulation results.

Appendix A

Phonon energies

The energies of phonons calculated from $S_1(\mathbf{q},\omega)$ in the bcc phase of ^{4}He (molar volume 21 cm^3) and ^{3}He (molar volume 21.5 cm^3) at T = 1.6 K are listed in Tabs. A.2-A.3. The phonon energy, ω, is in units of Kelvin, and the reciprocal lattice vector, q, is in relative lattice units (r.l.u.= $2\pi/a$, where $a = 4.1486\mathring{A}$ is the lattice parameter).

Table A.1: Calculated phonon energies ω(K) of the L[011], T_1[011] and T_2[011] phonon branches of bcc ^{4}He obtained by using $S_1(\mathbf{q},\omega)$.

q (r.l.u)	L[011]	T_1[011]	T_2[011]
0.20	16.2 ± 2.0	5.1 ± 1.2	10.1 ± 1.3
0.25	33.3 ± 2.3	5.1 ± 1.7	12.1 ± 1.3
0.29	21.2 ± 2.7	6.0 ± 1.7	12.1 ± 1.0
0.33	26.3 ± 1.5	6.05 ± 1.1	14.2 ± 2.0
0.40	29.3 ± 1.9	6.11 ± 1.0	15.2 ± 1.5
0.43	26.3 ± 2.8	6.1 ± 1.6	16.2 ± 2.5
0.50	31.3 ± 2.5	6.12 ± 2.4	15.2 ± 1.8

Footnote: In our recent simulations we have tried to detect new optic-like excitations in a strongly disordered sample of ^{4}He (bcc phase). We have calculated the $S(\mathbf{q},\omega)$ for

Table A.2: Calculated phonon energies, ω(K), of the L[001], T[001], L[111] and T[111] phonon branches of bcc ^{4}He obtained by using $S_1(\mathbf{q},\omega)$.

q (r.l.u)	L[001]	T[001]	L[111]	T[111]
0.14	7.1 ± 1.9	6.1 ± 1.0	16.2 ± 1.5	6.1 ± 1.9
0.20	9.1 ± 2.5	8.1 ± 1.5	20.2 ± 2.8	8.1 ± 0.0
0.25	12.1 ± 1.5	9.1 ± 1.8	21.2 ± 2.2	10.1 ± 1.8
0.29	13.1 ± 1.6	10.1 ± 1.5	22.2 ± 4.0	10.1 ± 1.5
0.33	15.5 ± 1.4	12.1 ± 1.0	22.2 ± 1.2	13.1 ± 1.8
0.40	16.2 ± 1.6	13.1 ± 1.1	23.2 ± 2.7	15.2 ± 2.1
0.43	18.2 ± 1.5	15.2 ± 1.8	23.2 ± 3.4	16.2 ± 3.0
0.50	19.2 ± 1.1	16.2 ± 1.2	18.2 ± 1.9	18.2 ± 2.2
0.57	18.2 ± 1.4	18.2 ± 1.5	14.2 ± 4.1	20.2 ± 2.2
0.60	20.2 ± 1.7	19.2 ± 0.9	11.1 ± 2.0	20.2 ± 2.8
0.67	21.2 ± 1.7	19.2 ± 1.8	9.1 ± 2.0	22.2 ± 3.4
0.71	21.2 ± 1.9	20.2 ± 1.9	10.1 ± 1.7	22.2 ± 4.2
0.75	21.2 ± 2.2	20.2 ± 1.9	13.1 ± 1.7	21.2 ± 3.6
0.80	21.2 ± 2.2	21.2 ± 2.4	15.2 ± 1.7	22.2 ± 2.3
0.83	22.4 ± 1.7	22.5 ± 2.3	18.2 ± 1.6	24.2 ± 4.1
0.86	21.2 ± 2.6	22.2 ± 2.5	22.2 ± 1.8	23.2 ± 3.1

a sample with 128 atoms, which contains 32 self-interstitial at the constant density (ρ = 0.02854 $1/\mathring{A}^3$) or the fixed volume (lattice constant $a = 4.1486\mathring{A}$). Unfortunately, despite of the large number of the measurements ($\sim$ 600,000), we have not be able to detect reliably the optic-like excitations. The significant fluctuations in the position of the additional features (the secondary peaks) of the $S(\mathbf{q},\omega)$ ruled out the unambiguous resolution of the new excitation modes.

Table A.3: Calculated phonon energies ω(K) of the L[011], T_2[011] and T_1[011] phonon branches of ^{3}He obtained by using $S_1(\mathbf{q},\omega)$.

q (r.l.u)	L[011]	T_2[011]	T_1[011]
0.17	18.5 ± 1.7	1.8 ± 1.5	10.0 ± 0.7
0.20	20.9 ± 0.5	2.8 ± 3.8	11.2 ± 0.3
0.25	24.2 ± 1.0	6.1 ± 2.8	13.1 ± 0.6
0.33	30.1 ± 1.6	7.1 ± 0.5	15.8 ± 0.7
0.40	32.0 ± 2.5	7.1 ± 0.0	17.2 ± 0.4
0.50	32.4 ± 2.0	8.1 ± 2.5	17.6 ± 1.1

Table A.4: Calculated phonon energies ω(K) of the L[001], T[001], L[111] and T[111] phonon branches of bcc ^{3}He obtained by using $S_1(\mathbf{q},\omega)$.

q (r.l.u)	L[001]	T[001]	L[111]	T[111]
0.20	12.6 ± 0.5	8.7 ± 0.5	19.2 ± 2.9	9.7 ± 0.4
0.25	15.8 ± 0.5	10.5 ± 0.5	24.5 ± 3.1	11.7 ± 0.6
0.33	17.0 ± 1.6	11.9 ± 1.1	23.9 ± 3.9	14.3 ± 1.7
0.40	22.0 ± 1.2	15.9 ± 0.5	25.8 ± 4.7	18.4 ± 0.8
0.50	23.6 ± 0.6	18.9 ± 0.9	21.3 ± 1.1	21.9 ± 1.5
0.60	22.1 ± 1.5	21.3 ± 1.0	13.5 ± 1.5	24.7 ± 2.1
0.67	23.5 ± 2.4	22.0 ± 1.7	11.9 ± 0.7	25.8 ± 3.5
0.75	23.5 ± 1.6	24.5 ± 1.1	15.8 ± 3.1	24.3 ± 2.1
0.80	24.9 ± 0.9	25.5 ± 2.0	15.0 ± 3.6	24.7 ± 1.9
0.83	24.6 ± 1.4	25.2 ± 1.2	19.4 ± 4.1	25.2 ± 2.1
1.00	26.6 ± 0.8	25.4 ± 1.3	25.7 ± 0.7	25.7 ± 2.7

Appendix B

Melting curves

The melting curves for bulk, Ar(001) and Ar(011) with soft and rigid boundaries are listed in Tabs. B.1 and B.2. The T_m is in units of Kelvin, and the pressure in GPa.

Table B.1: Melting temperature $T_m(K)$ as a function of pressure P for the surface-free sample (bulk) and the samples (Ar) bordered by hard walls with different surface geometry.

P (GPa)	bulk	Ar(011)	Ar(001)
1.04	300 ± 10	285 ± 10	300 ± 10
2.08	470 ± 10	440 ± 10	480 ± 10
4.16	780 ± 10	730 ± 10	780 ± 10
8.28	1250 ± 10	1200 ± 10	1340 ± 10
10.76	1530 ± 10	1400 ± 10	1530 ± 10
12.82	1710 ± 5.0	1710 ±10	1735± 5.0
20.03	2415 ±10	2360 ±10	2510 ± 10
22.43	2645 ±10	2455 ±10	2730 ± 15
24.99	2860 ±10	2770 ±10	2930 ± 10
29.96	3280± 20	3100 ±10	3325 ± 10

Table B.2: Melting temperature $T_m(K)$ as a function of pressure P for the surface-free sample (bulk) and the samples (ArNe) bordered by neon layers with different surface geometry.

P (GPa)	Bulk	ArNe (011)	ArNe (001)
1.04	300 ± 10	250 ± 10	250 ± 10
2.08	470 ± 10	440 ± 10	390 ± 10
4.16	780 ± 10	635 ± 10	665 ± 10
8.28	1250 ± 10	1020 ± 10	1040 ± 20
10.76	1530 ± 10	1180 ± 10	1230 ± 20
12.82	1710 ± 5.0	1380 ± 10	1640 ±10
20.03	2415 ±10	1975 ± 10	2020 ±20
22.43	2645 ±10	2137 ± 12	2225 ±15
24.99	2860 ±10	2315 ± 15	2335 ±15
29.96	3280± 20	2680 ± 10	2675 ±20

References

[1] H. R. Glyde, *Excitations in Liquid and Solid Helium* , Clarendon Press, Oxford, (1994).

[2] D. M. Ceperley, Rev. Mod. Phys.,**67**, 279 (1995)

[3] H. R. Glyde and F. C. Khanna, Can. J. Phys., **49**, 2997, (1971).

[4] D. Errandonea, Physica B, **357**, 356 (2005). D. Errandonea, B. Schwager, R. Ditz, C. Gessmann, R. Boehler, and M. Ross Phys. Rev. B **63**, 132104 (2001).

[5] J.G. Dash, Rev. of Mod. Phys. **71**, 71 (1999).

[6] U. Tartaglino, T. Zykova-Timan, F. Ercolessi and E. Tossati, Phy. Rep. **411**, 291 (2005).

[7] E. Kim and M. H. W. Chan, Science, **305**, 1941 (2004).

[8] T. Markovich, E. Polturak, J. Bossy, and E. Farhi, Phys. Rev. Lett., **88**, 195301 (2002).

[9] T. Markovich, *Inelastic-Neutron Scattering from bcc* ^{4}*He*, PhD. Thesis, Haifa, Technion, (2001).

[10] O.Pelleg and E. Polturak, oral talk in Condensed Matter session at IPS 2005 (Carmiel), submitted to PRB, Rapid Communications

[11] N. Gov and E. Polturak, Phys. Rev. **B** , **60**, 1019 (1999).

[12] M. Boninsegni and D. M. Ceperley, J. Low. Temp. Phys. **104**, 336 (1996).

[13] D. E. Galli and L. Reatto, J. Low. Temp. Phys., **134**, 121 (2004).

[14] F. Lindemann, Z.Phys, **11**, 609 (1910).

[15] F. W. de Wette and B. R. A. Nijboer, Phys. Lett.,**18**, 19 (1965).

[16] M. Born, Journ. of Chem. Phys., **7**, 591 (1939).

[17] E. B. Osgood, V. J. Minkiewicz, T. A. Kitchens, and G. Shirane, Phys. Rev. A **5**, 1537 (1972).

[18] E. B. Osgood, V. J. Minkiewicz, T. A. Kitchens, and G. Shirane, Phys. Rev. A **6**, 526 (1972).

[19] V. J. Minkiewicz, T. A. Kitchens, G. Shirane, and E. B. Osgood, Phys. Rev. A **8**, 1513 (1973).

[20] H. R. Glyde, Can. J. Phys.**49**, 761 (1971).

[21] H. R. Glyde, J. Low. Temp. Phys., **3**, 559 (1970).

[22] H. R. Glyde, Can. J. Phys.**49**, 2997 (1971).

[23] T. R. Koehler and N. R. Werthamer, Phys. Rev. A **3**, 2074 (1971).

[24] R. P. Feynman, Phys. Rev.**91**, 1301 (1953).

[25] G. Meissner, Z. Physics, **205**, 249 (1967).

[26] D. R. Fredkin and N. R. Werthamer, Phys. Rev. A **138**, 1527 (1965).

[27] V. Tozzini and M. P. Tosi, Physica B, **262**, 369 (1999).

[28] H. Horner, J. Low. Temp. Phys. **8**, 511 (1972).

[29] H. Horner, Phys. Rev. Let.,**29**, 556 (1972).

[30] E. R. Dobbs, Solid Helium Three (Oxford University Press, Oxford,1994).

[31] R. Senesi, C. Andreani, D. Colognesi, A. Cunsolo and M. Nardone, Phys. Rev. Lett. **86** , 4584 (2001).

[32] C. Seyfert, R. Simmons, H. Sinn, D. Armss and E. Burkel, J. Cond. Matt. **11**, 3501, (1999)

[33] E. Burkel,C. Seyfert,C. Halcoussis,H. Sinn, and R. O. Simmons, Physica B. **263**, 412, (1999)

[34] S. Schottl, K. Siemensmeyer, V. Boyko, I. Batko,S Matias, S. Raasch, E. D. Adams, and T. E. Sherline, J. Low Temp. Phys., **126**, 51, (2002)

[35] R. Schanen, T. E. Sherline, A. M. Toader, V. Boyko, S. Matas, M. Meschke, S. Schottl, E. D. Adams, B. Cowan, H. Godfrin, J.P. Goff, M. Roger, J. Saunders, K. Siemensmeyer, and Y. Takano, Physica B., **329**, 392, (2003)

[36] H. Horner, Phys. Rev. Lett., **25**, 147, (1970).

[37] B. Clark and D. M. Ceperley,
http : *//www.physics.uiuc.edu/People/Faculty/Ceperley/papers/index.htm*

[38] *Rare gas solids* edited by M. L. Klein and J. A. Venables Academic Press, London, 1976

[39] B. Bernu and D. M. Ceperley, in *Quantum Simulations of Complex Many-Body Systems: From Theory to Algorithms* , Lecture Notes p.51, NIC Series Vol. 10, Julich, 2002

[40] R. P. Feynman, *Statistical Mechanics* , Benjamin, New York, 1972

[41] A. Nakayama and N. Makri, PNAS, **192**, 4230 (2005).

[42] R. A. Aziz, A. R. Janzen, and M. R. Moldover, Phys. Rev. Let. **74**, 1586 (1995).

[43] M. Born and K. Huang, *Dynamical theory of crystal lattices*, Clarendon Press, Oxford, (1954).

[44] P. Bruesch,*Phonons, theory and experiments I : lattice dynamics and models of inter atomic forces* , Berlin, Springer, (1982).

[45] M. Jarrell and J. E. Gubernatis, Phys. Rep., **269**, 133 (1996).

[46] E. W. Draeger and D. M. Ceperley, Phys. Rev. B **61**, 12094 (2000).

[47] B. Chaudhuri, F. Pederiva, and G. V. Chester, Phys. Rev. B., **60**, 3271 (1999).

[48] D. S. Greywall, Phys. Rev. B, **11**, 1070, (1975).

[49] F. Pederiva, G. V. Chester, S. Fantoni, and L. Reatto, Phys. Rev. B **56**, 5909, (1997).

[50] C. A. Burns and J. M. Goodkind, J. Low. Temp. Phys., **95**, 695 (1994).

[51] A. R. Allen, M. G. Richards, and G. Sharter, J. Low. Temp. Phys., **47** 289 (1982).

[52] I. Schuster, E. Polturak, Y. Swirsky, E. J. Schmidt, and S. G. Lipson, J. Low Temp. Phys. **103**, 159 (1996).

[53] B. A. Fraass, P. R. Granfors, and R. O. Simmons, Phys. Rev. B., **39**, 124 (1989).

[54] A. Jayaraman, Rev. Mod. Phys. **55**, 65 (1983).

[55] G. E. Duvall and R. A. Graham, Rev. Mod. Phys. **49**, 523 (1977).

[56] S. N. Luo, A. Strachan, and D. C. Swift, J. of Chem. Phys. **120**, 11640 (2004).

[57] S. Japel, B. Schwanger, R. Boehler, and M. Ross, Phys. Rev. Let., **95**, 167801 (2005).

[58] D. Alfe, L. Vocaldo, G. D. Price and M. J. Gillan, J. Phys.: Condens. Matter, **16**, S973 (2004).

[59] G. Shen, *www.gsecars.org/ shen/shen/publication/Shen − ency*2005.*pdf*

[60] N. Holmes, *http* : *//www.llnl.gov/str/Holmes.html*

[61] K. Kadai, T. C. Germann, P. S. Lomdahl, and B. L. Holian, Science, **296**, 1681 (2002).

[62] L. Burakovsky, D. L. Preston, and R. R. Silbar, Phys. Rev. B **61**, 15011 (2000).

[63] L. Burakovsky, D. L. Preston, and R. R. Silbar, J. Appl. Phys. **88**, 6294 (2000).

[64] A. R. Ubbeldone, Melting and Crystal Structure, Clarendon press, (Oxford) 1965

[65] F. Lindemann, Z.Phys. **11**, 609 (1910).

[66] M. Born, Jour. Chem. Phys. **7**, 591 (1939).

[67] A.V. Granato, Phys. Rev. Lett. **68**, 974 (1992).

[68] R. W. Cahn, Nature **323**, 668 (1986).

[69] V. Sorkin, E. Polturak and Joan Adler, Phys. Rev. B **68**, 174102 (2003).

[70] V. V. Kechin, Phys. Rev. B **65**, 052102 (2002).

[71] R. M. J. Cotterill, Phys. Rev. Lett. **42**, 1541 (1979).

[72] L. Gomez, A. Dobry, Geuting, H. T. Diep, and L. Burakovsky, Phys. Rev. Lett. **90**, 095701 (2003)

[73] L. Gomez, C. Gazza, H. Dacharry, L. Penaranda, and A. Dobry, Phys. Rev. B **71**, 134106 (2005).

[74] D. A. Young and M. Ross, J. Chem. Phys. **15**, 6950 (1981).

[75] A. B. Belonoshko, Science, **275**, 955 (1992).

[76] A. B. Belonoshko, High Press. Res., **10**, 583 (1992).

[77] D. Frenkel and B. Smit, *Understanding molecular simulations*, Academic Press, San Diego, 1996

[78] J. R. Morris, C. Z. Wang, K. M. Ho, and C. T. Chan, Phys. Rev. B **49**, 3109 (1994).

[79] Xian-Ming Bai and Mo Li, Phys. Rev. B **72**, 052108 (2005).

[80] K. Lu and Y. Li, Phys. Rev. Lett. **80**, 4474 (1998).

[81] G. S. Heffelfinger and M. E. Lewitt, J. of Comp. Chem., **17**, 250 (1996).

[82] *Rare gas solids* edited by M. L. Klein and J. A. Venables Academic Press, London,1976

[83] L. E. Reichl *A Modern Course in Statistical Physics*, A Willey-Interscience Publication, New York,1998

[84] Handbook of Chemistry and Physics, 81'st edition 2000-2001 year, D. R. Lide, editor in chief, CRC Press

[85] Pathria R. K. *Statistical Mechanics*, Elsevier Science and Technology Books, San Diego, 1996

[86] J. Adler, A. Hashibon, N. Schreiber, A. Sorkin, S. Sorkin and G. Wagner, Comp. Phys. Comm. **12, No.5**, 623 (2002).

[87] J. Adler, Computers in Science and Engineering, **5**, 61 , (2003).

[88] J. Daeges, H. Geiter and J. H. Peperezko, Phys. Lett. A, **119**, 79 (1986).

[89] G. I. Kanel, S. V. Razorenov and V. E. Fortov, J. Phys.: Condens. Matter, **16**, S1007 (2004).

[90] C. J. Rossouw and S. E. Donnelly, Phys. Rev. Lett. **55**, 2960 (1985).

[91] F. Datchi, P. Loubeyre and R. Le Toullec, Phys. Rev. B, **61**, 6535 (2000).

[92] R. Boehler, M. Ross, P. Soderlind, and D. B. Boecker, Phys. Rev. Lett., **86**, 5731 (2001).